Order Number 9405608

Electron-photon polarization correlation study of Ne, Ar and Kr excitation by electron impact

Zheng, Shuanghai, Ph.D.

City University of New York, 1993

U·M·I
300 N. Zeeb Rd.
Ann Arbor, MI 48106

A

Electron-Photon Polarization Correlation Study of Ne, Ar and Kr Excitation by Electron Impact

by

Shuanghai Zheng

A dissertation submitted to the Graduate faculty in Physics in partial fulfillment of the requirements for the degree of Doctor of Philosophy, the City University of New York

1993

This manuscript has been read and accepted for the Graduate Faculty in Physics in satisfaction of the dissertation requirement for the degree of Doctor of Philosophy.

5/28/93
Date

Chair of the Examining Committee
Professor Kurt H. Becker

6/2/93
Date

co-chair of the Examining Committee
Professor Marvin H. Mittleman

5/28/93
Date

Executive Officer
Professor J. B. Krieger

Professor Ngee-Pong Chang

Professor Marten Den Boer

Professor Michael S. Lubell

Supervisory Committee

The City University of New York

Abstract

Electron-Photon Polarization Correlation Study of
Ne, Ar and Kr Excitation by Electron Impact

by

Shuanghai Zheng

Advisor: Kurt H. Becker

The electron impact excitation of the $3s'[1/2]^0_1$ state in neon, the $4s'[1/2]^0_1$ state in argon and the $5s[3/2]^0_1$ state in krypton have been studied using the electron-photon polarization correlation technique. The two linear coherence parameters P_1 and P_2 have been measured and the alignment angle γ and the linear polarization P^+_{lin} of the angular part of the collisionally induced excited state charge cloud were extracted from the measured P_1 and P_2 parameters. We measured P_1 and P_2 in neon at an impact energy of 50 eV, in argon at impact energies of 50 eV, 40 eV, 30 eV and 25 eV, and in krypton at impact energies of 50 eV and 30 eV and electron scattering angles up to 55° in all cases. A comparison with theoretical predictions from first-order perturbative theories such as a Distorted Wave Born Approximation (DWBA) and a First Order Many Body Theory (FOMBT) was made. At 50 eV in neon and argon, the agreement between experiment and theory is generally good at small scattering angles up to 25° and somewhat poorer at larger scattering angles. At 50 eV in krypton, the agreement between experiment and theory is generally good at scattering angles up to 40°. The measurements in argon (40 eV, 30 eV, and 25 eV) generally follow the trend of the theoretical predictions, but it was found that the

experimentally measured coherence parameters appear to be shifted towards larger scattering angles compared to the theoretical predictions as the impact energy is decreased. At 30 eV in krypton, very good agreement between experiment and theory was found over the entire range of electron scattering angles (up to 55°). The level of agreement between experiment and theory indicates that the DWBA and FOMBT appear to provide a better description of the collision process for a more complex target. We also found that the alignment angle γ is the parameter which is perhaps least sensitive to the details of the collision.

Acknowledgments

I greatly appreciate the patient guidance, assistance, encouragement, and help of my advisor, Professor Kurt H. Becker, during the course of this thesis work. I would especially like to acknowledge Professor Kurt H. Becker for giving me an opportunity to study with him during a critical period in my career.

It is a great pleasure to thank Dr. K. Martus for his patient guidance in introducing me to the experimental details of the electron and photon technique. Special thanks must go to Professor Ngee-Pong Chang who nurtured my interest in and understanding of physics.

I would like to thank Dr. V. Tarnovsky and Mr. R. Siegel for many helpful discussions, for their assistance and their encouragement and I would also like to thank Mr. J. Altmann and his staff in the machine shop and Mr. F. Du in the electronics shop for their assistance in modifying and machining the apparatus. I am grateful to Professor K. Bartschat and Professor D. H. Madison for providing us with some unpublished DWBA calculations. I wish to thank Professor F. Liu for his constant encouragement during the entire period of the preparation of this thesis.

I like to dedicate this thesis to my wife Jing and my daughter Joan and sincerely thank them for their spiritual support, especially during a difficult period in our family life in the final stages of the preparation of this thesis.

Table of Contents

Abstract iii

Acknowledgments v

Table of Contents vi

Chapter 1 Introduction 1

Chapter 2 Background 4

2.1 Historical Background 4

2.2 Basic Experimental Details 7

2.3 Conceptual Description of the Measured Quantities 11

Chapter 3 Theoretical Details 15

3.1 Basic Concepts 15

3.2 The Polarization of the Emitted Light 22

3.3 The Distorted Wave Born Approximation (DWBA) 30

3.4 The First Order Many Body Theory (FOMBT) 35

Chapter 4 Experimental Details 36

4.1 The Vacuum System 38

4.2 The Electron Spectrometer 40

4.3 The Gas Beam 43

4.4 Polarization Analysis in the VUV 45

Chapter 5 Experimental Procedure 48

5.1 Operation of the Electron Spectrometer 48

5.2 The Alignment of the Electron Beam and the Calibration of the Scattering Angle 54

5.3 Operation of VUV Reflection Polarization Analyzer 59

5.4 Data Acquisition 62

Chapter 6 The Instrumental Effects 71

6.1 The Depolarization due to the Hyperfine Structure 72

6.2 The Depolarization due to Instrumental Effects 75

Chapter 7 Experimental Results and Discussion 78

7.1 Excitation of the $ns'[1/2]^0_1$ State in Ne (n=3) and Ar (n=4) and of the $5s[3/2]^0_1$ State in Kr at 50 eV 79

7.2 Excitation of the $4s'[1/2]^0_1$ State in Ar at 50 eV, 40 eV, 30 eV and 25 eV 94

7.3 Excitation of the $5s[3/2]^0_1$ State in Kr at 30 eV 107

7.4 Summary and Future Directions 112

Figures

2.2.1 8

2.2.2 9

2.2.3 10

2.3.1 12

5.1.1 49

5.1.2 52

5.2.1 56

5.3.1 60

5.4.1 63

5.4.2 64

5.4.3 67

Figures of the Experimental Data

7.1.1 80

7.1.2 82

7.1.3 85

7.1.4 87

7.1.5 89

7.1.6 92

7.2.1 95

7.2.2 100

7.2.3 96

7.2.4 101

7.2.5 97

7.2.6 102

7.3.1 108

7.3.2 109

Tables

3.1.1 16

6.1.1 73

Tables of the Experimental Data

7.1.1 84

7.1.2 88

7.1.3 91

7.2.1 104

7.2.2 105

7.2.3 106

7.3.1 111

Bibliography 114

Chapter 1 Introduction

Electron-atom collisions have played a prominent role in atomic physics since the beginning of this century. Electron scattering is a sensitive tool to probe the structure of an atom as well as the dynamics of the collision process. The first electron collision experiment of Franck and Hertz in 1914, which demonstrated the existence of discrete energy levels in atoms, opened the door to almost eighty years of experimental and theoretical activities which have provided us with a detailed understanding of atomic structure and of the dynamics of the interaction of an atom with a charged particle.

The early days of electron collision physics provided some striking examples of the quantum mechanical nature of scattering processes, e.g. the Ramsauer-Townsend effect [Ramsauer 1921a, 1921b, Townsend and Bailey 1922]. Most electron collision studies in those days focused on total cross section measurements for both elastic as well as inelastic electron collisions. During the period from before the Second World War until a few years after the war, atomic physics and electron collision physics along with it played only a secondary role behind the then rapidly developing field of nuclear physics. A second, very active period of electron collisions research followed in the 1950s and 1960s with intensive experimental and theoretical work done in the areas of differential cross section measurements, the study of resonance phenomena and the measurement of the polarization of the light emitted by electron-impact excited atoms.

The early 1970s marked the beginning of a new era in electron collision physics. The concept of a "complete" or "perfect" scattering experiment emerged

[Bederson 1969, 1973], a scattering experiment in which one would like to obtain all relevant quantum numbers of the collision complex "projectile + target" both before and after the collision. Advances in experimental techniques and novel instrumentation (for example, the application of angular correlation techniques to electron-atom scattering processes, the development of polarized-electron sources and the use of laser techniques to prepare atoms in well- defined quantum states) enabled experiments to make great progress towards the achievement of a perfect scattering experiment. Even though to date a complete scattering experiment has only been performed for elastic scattering [see e.g. Kessler 1991], electron-photon coincidence studies of inelastic electron collision processes provide detailed information at the level of quantum mechanical excitation amplitudes and their interference (coherence parameters), rather than at the level of moduli squared amplitudes (cross sections). The principle of an electron- photon coincidence experiment consists of the time- correlated (coincident) detection of inelastically scattered electrons which have excited a particular target state and the subsequently emitted decay photons. This can be done either without regard for the light polarization (angular correlation measurements) or after a linear and/or circular polarization analysis of the emitted radiation has been performed (polarization correlation measurements).

The first electron-photon coincidence experiments were carried out by Kleinpoppen and collaborators [Eminyan et al. 1973, 1974] who used the angular correlation technique to probe the excitation of the 2^1P and 3^1P states of He from the 1^1S ground state. Helium, in particular the excitation of the n^1P states, remained the favorite target of both experimentalists and theorists for many years. More recently, the emphasis has shifted to the study of the excitation of states with higher orbital

angular momentum quantum numbers, to the excitation of triplet states (from a singlet ground state) and to more complex targets such as atomic hydrogen, sodium, mercury and the heavy noble gases. The heavy noble gases, in particular, have been the target of extensive studies using both the angular correlation technique as well as the polarization correlation technique in recent years. The atomic structure of the heavy noble gases is still comparatively simple and well-understood, the data analysis is largely free from complications such as hyperfine depolarization effects and one can hope to reveal systematic Z-dependent trends and tendencies in the data as one goes from the lightest heavy noble gas atom, Ne, to Ar to Kr to Xe (here Z stands for the nuclear charge). The experiments carried out as part of the present thesis are polarization correlation measurements with the heavy noble gas atoms Ne, Ar and Kr as targets, predominantly in the scattering regime of large impact parameters.

Alternate experimental approaches to the measurement of coherence parameters do exist, such as the super-elastic scattering from laser-excited atoms [Hertel and Stoll 1974] and offer, in fact, experimental advantages over electron-photon coincidence experiments. Such studies are, however, confined to target states that can be prepared by currently available lasers. Very recently, the first results have been reported for electron-photon coincidence studies carried out with spin-polarized incident electrons in Hg [Sohn and Hanne 1992] and in Xe [Uhrig et al 1993]. One can hope that such experiments will provide an even more detailed understanding of the role of spin-effects in inelastic electron collision processes.

Chapter 2 Background

§2.1 Historical Background

The earliest electron-atom collision experiments are those of Franck and Hertz [1914]. Subsequently, many experiments measured electron-impact cross sections, which represent the moduli squared scattering amplitudes, and which are the traditional physical quantities measured in an electron-atom collision experiment, both for elastic and inelastic collisions. For inelastic collisions, the ratio for the excitation of different magnetic sublevels can be extracted from a measurement of the linear polarization of the collisionally induced light emission [e.g. Moiseiwitsch and Smith 1968, Heddle and Gallagher 1989]. More detailed information such as information about individual excitation amplitudes and their interference can be obtained from electron-photon coincidence experiments, i.e. from the measurement of the so-called coherence parameters which along with the cross section provide a complete description of the inelastic electron-atom collision process except for certain spin variables which can only be obtained from experiments using spin-polarized particles.

The theoretical groundwork for the description of electron-photon coincidence experiment has been laid by Rubin et al. [1969], Macek and Jaecks [1971], Wykes [1972], and in the review paper of Fano and Macek [1973] which is considered the most fundamental paper. Various equivalent sets of coherence parameters have been introduced, i.e. the Blum-da Paixao parameters [da Paixao et al. 1980], the alignment and orientation parameters of Fano and Macek [1973] and the Stokes´ parameters. Recently, Andersen et al. [1988] introduced a set of frame-independent parameters, the natural parameters (γ , $L_\perp$, P_{lin}^{+}, ρ_{00}), which are now widely accepted as the

standard coherence parameters. (A more detailed description of these parameters will be given later.)

Theoretical predictions for coherence parameters describing the excitation of the $ns'[1/2]^0_1$ and $ns[3/2]^0_1$ states (Racah notation) of the noble gases have utilized first order perturbation approximations, such as the Distorted-Wave-Born-Approximation (DWBA) [Bartschat and Madison 1987] and the First-Order-Many-Body-Theory (FOMBT) [Machado et al. 1982, 1984, 1991, da Paixao et al 1984, Meneses et al 1985, 1991]. In addition, Zuo et al. (1991) performed a Relativistic Distorted Wave (RDW) calculation.

The first experimental electron-photon-coincidence studies were carried out by Kleinpoppen and collaborators [Eminyan et al. 1973, 1974], who measured electron-photon angular correlations for the excitation of the 2^1P and 3^1P states in helium from the ground state. Measurements in the heavy noble gases have been carried out using either angular correlation techniques [Arriola et al. 1975, Ugabe et al. 1977, Pochat 1980, McGregor et al. 1982, King et al. 1985, Dano et al. 1985, Nishimura et al. 1986, Murray et al. 1990] or polarization correlation technique [Malcolm and McConkey 1979, Khakoo and McConkey 1986, 1987, Beijers et al. 1987, Martus and Becker 1989,Corr et al. 1990, 1991, Martus et al. 1991, Zheng and Becker 1992, 1993]. In principle, only three of the required four coherence parameters can be extracted from an angular correlation experiment as will be shown later.

Since the wavelength of resonance radiation of the heavy noble gases is in the vacuum ultraviolet (VUV), the electron-polarized photon coincidence experiments did not become feasible until techniques for linear and circular polarization analysis for VUV light had been fully established [Samson 1967, McConkey et al. 1982, Zetner

et al. 1983, 1984, Westerveld et al. 1985]. Since Malcolm and McConkey [1979] and Khakoo and McConkey [1986] reported the first measurements of the polarization correlation parameters for the $ns'[1/2]^0_1$ state in Ar at 50 eV and 80 eV, a wealth of experimental polarization correlation data has been accumulated, and detailed comparisons with theoretical predictions have been carried out [see the review papers by Andersen et al. 1988, Slevin and Chwirot 1990, Becker et al 1992].

§2.2 Basic Experimental Details

An electron beam of fixed energy (20 - 200eV) produced by an electron monochromator intersects a beam of heavy noble gas atoms (Ne, Ar, Kr) emanating from a single hypodermic needle. An electron energy analyzer located at a scattering angle Θ_e in conjunction with a channel electron multiplier (CEM) detects those electrons that have lost an amount of energy which corresponds to the energy necessary to excite a particular state in Ne, Ar or Kr. The atom subsequently emits a decay photon whose polarization is also analyzed. In the case of the $ns'[1/2]^0_1$ and $ns[3/2]^0_1$ states of the heavy noble gases, the wavelengths of the decay photons are in the VUV. As a consequence, reflection optics rather than transmission optics are required for the polarization analysis. Gold coated, optically flat mirrors (one mirror for a linear polarization analysis, two mirrors for a circular polarization analysis) in conjunction with another CEM are employed as polarization sensitive photon detectors. Coincidences between the inelastically scattered electrons and the photons whose polarization is also analyzed are recorded.

A schematic diagram of the electron-polarized photon coincidence apparatus is shown in figure 2.2.1.

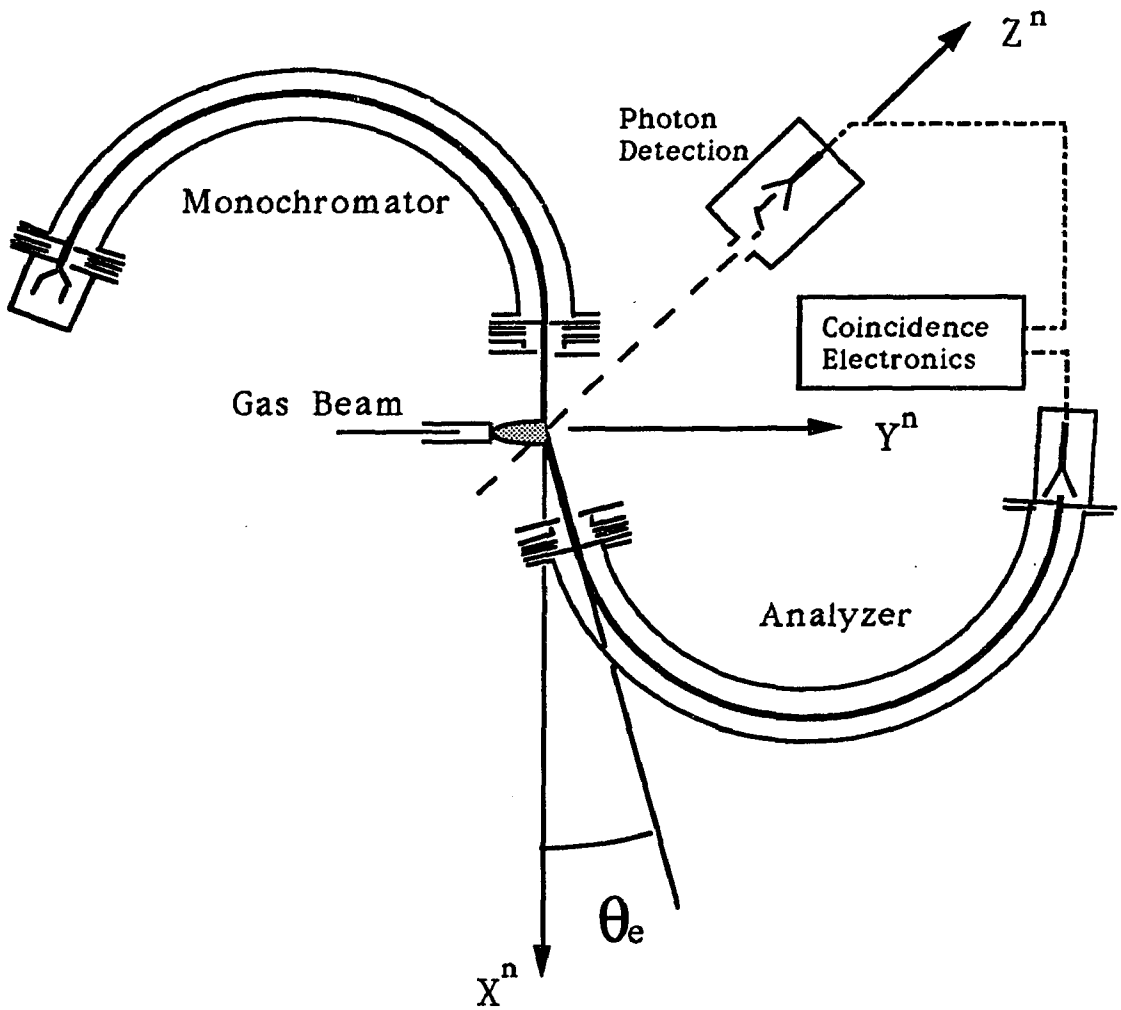

Figure 2.2.1: Schematic diagram of the experimental apparatus. The electron monochromator/analyzer, the gas beam, and the photon detector are inside a high vacuum chamber and in the (X^n, Y^n) plane. The description of electrostatic Einzel lenses of the electron monochromator and analyzer is given in figure 2.2.2 and in figure 2.2.3. The Z^n axis points out of the paper, so that (X^n, Y^n, Z^n) constructs a right-hand coordinate frame.

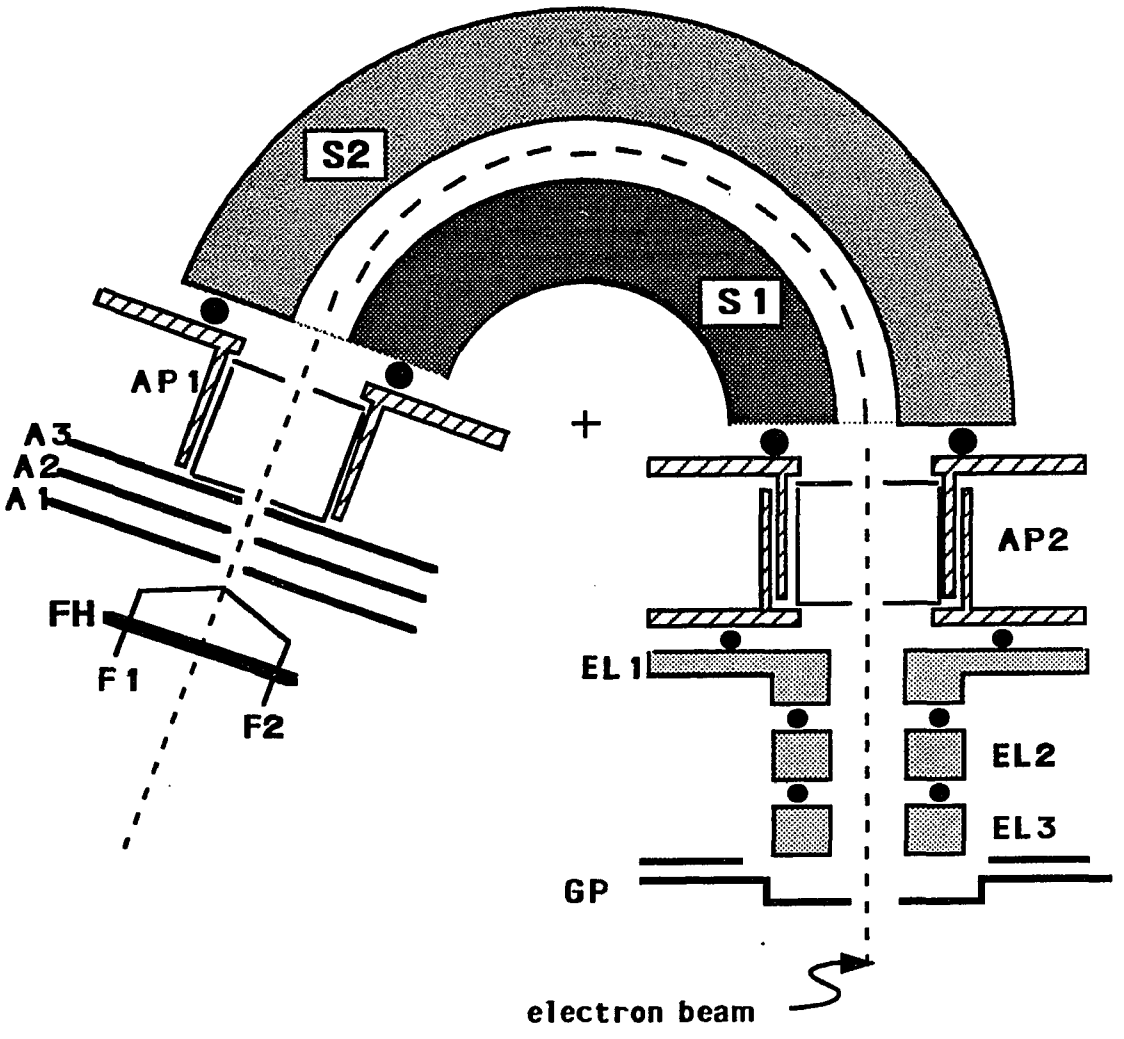

Figure 2.2.2: The essential parts of the electrostatic monochromator. The various components labeled in the figure will be discussed later.

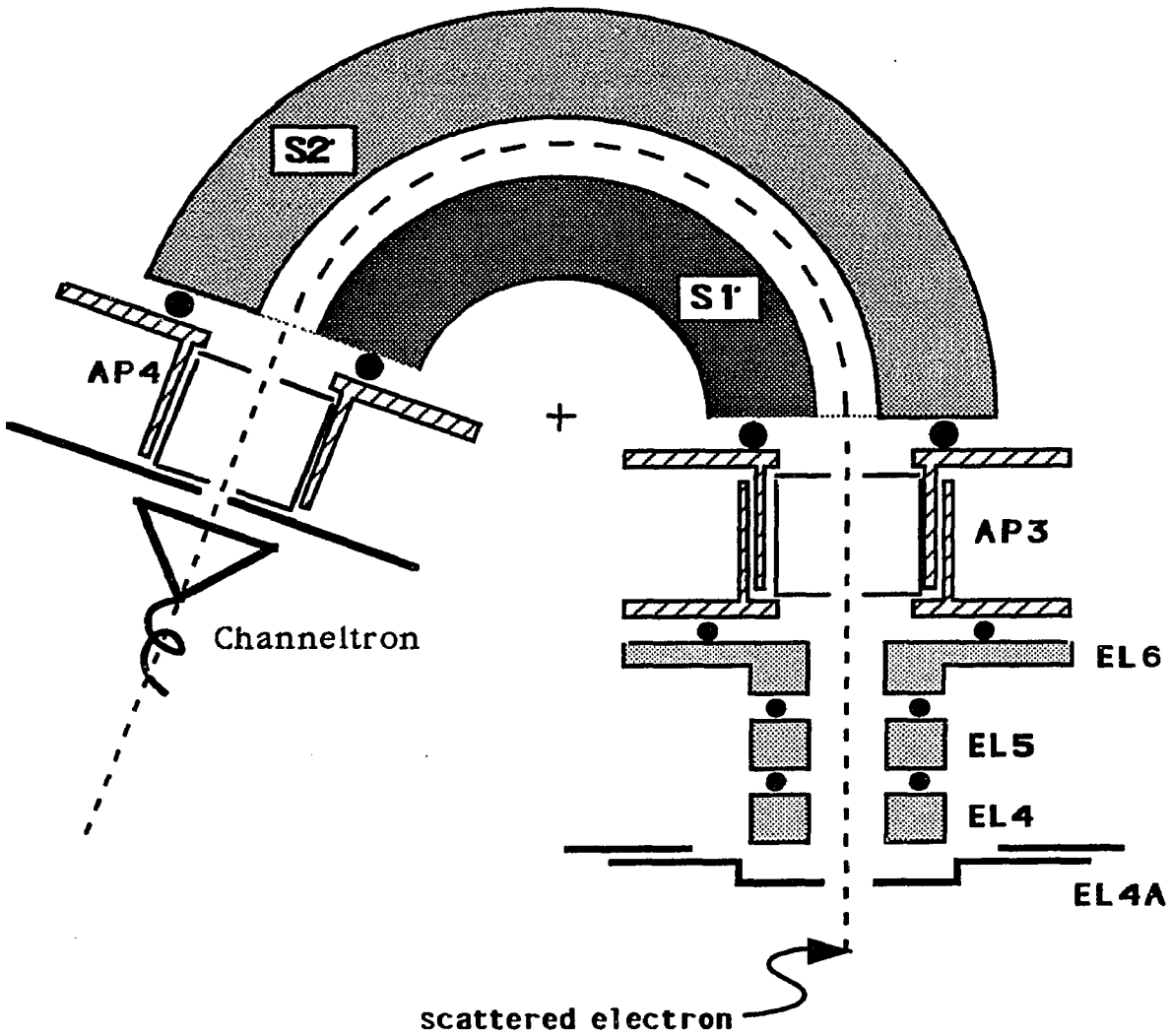

Figure 2.2.3: The essential parts of the electrostatic electron analyzer. The various components labeled in the figure will be discussed later.

§2.3 Conceptual Description of the Measured Quantities

Various reference frames have been introduced in the literature [Andersen et al. 1987] to describe the experiments that were carried out as part of this thesis.

(1) The *Collision Frame* (x^c, y^c, z^c): the z^c axis is chosen as the direction of the incoming electron momentum vector $\vec{k}_{in}$. $\vec{k}_{in}$ and $\vec{k}_{out}$, the momentum vector of the outgoing electron, define the (z^c, x^c) scattering plane. y^c is perpendicular to the scattering plane.

(2) The *Natural Frame* (x^n, y^n, z^n): which is related to the collision frame through $x^n \equiv z^c$, $y^n \equiv x^c$, $z^n \equiv y^c$.

(3) The *Atomic Frame* (x^a, y^a, z^a): whose axes are defined through $z^a \equiv z^n$, and x^a and y^a define the scattering plane with x^a being parallel to the symmetry axis of the atomic charge cloud.

The initial and the final state of the heavy noble gas atoms in our experiment is the $^1S_0$ ground state, which means that its electron charge cloud is isotropic. Only the electron charge cloud of the excited P-states provides any dynamical information about the excitation process.

The angular part of the collisionally induced excited state charge cloud is shown in figure 2.3.1.

The atomic charge cloud is fully characterized by three parameters [Andersen et al. 1988], the alignment angle γ, the relative height h and the relative length l (or relative width w with the condition $h + l + w = 1$). One additional parameter, $L_\perp$, is defined as the angular momentum along the direction perpendicular to the scattering plane transferred during the collision and is given in units of $\hbar$. $L_\perp$ is the angular

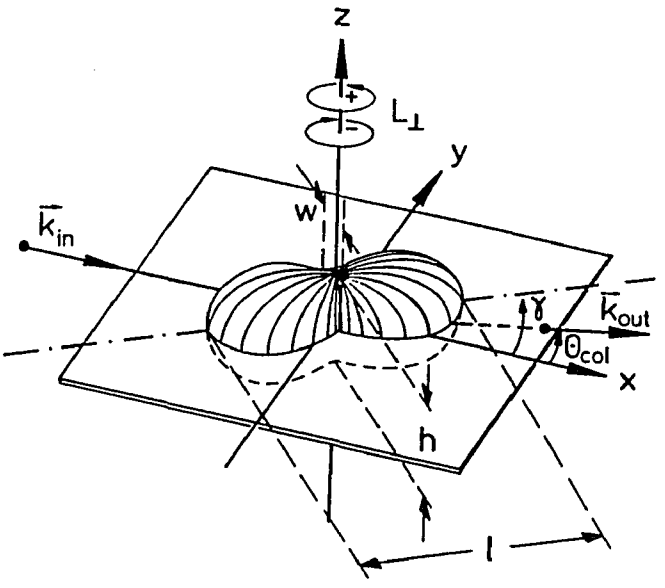

Figure 2.3.1: Schematic illustration of a collisionally induced charge cloud in a p-state atom. The scattering plane is fixed by the direction of incoming $\mathbf{k}_{in}$ and outgoing $\mathbf{k}_{out}$ relative momentum vector of the particles. The atom is characterized by the relative length (l) (or width (w)), and height (h), by its alignment angle γ and by its inherent angular momentum $L_\perp$. The coordinate frame given is the so-called natural frame with the z-axis perpendicular to the scattering plane and the x- and y-axis defined in the figure relative to $\mathbf{k}_{in}$ and $\mathbf{k}_{out}$.

momentum expectation value of the excited state of the atoms.

The polarization correlation or Stokes' parameters, which are directly measured in the electron-polarized photon coincidence experiment, are defined as follows:

i) In the direction perpendicular to the scattering plane, two linear polarization correlation parameters are defined as

$$P_1 = \frac{I_{(0°)} - I_{(90°)}}{I_{(0°)} + I_{(90°)}} \tag{2-3-1}$$

$$P_2 = \frac{I_{(45°)} - I_{(135°)}}{I_{(45°)} + I_{(135°)}} \tag{2-3-2}$$

Here $I_{(\phi)}$ is the coincident light intensity with linear polarization in a direction ϕ relative to the incoming electron beam.

In the direction perpendicular to the scattering plane, the circular polarization parameter is defined as

$$P_3 = \frac{I_{(\,RHC\,)} - I_{(\,LHC\,)}}{I_{(\,RHC\,)} + I_{(\,LHC\,)}} \tag{2-3-3}$$

where $I_{(\,RHC\,)}$ and $I_{(\,LHC\,)}$ are the coincident right-handed and left-handed circular light intensities, respectively.

ii) Another linear polarization parameter is defined in the direction perpendicular to the incoming electron beam and in the scattering plane as

$$P_4 = \frac{I_{(\,para\,)} - I_{(\,perp\,)}}{I_{(\,para\,)} + I_{(\,perp\,)}} \tag{2-3-4}$$

where $I_{(\,para\,)}$ and $I_{(\,perp\,)}$ are the coincident light intensities with the polarization vector in the direction parallel and perpendicular to the scattering plane.

The natural parameters (γ, $L_\perp$, P_{lin}^+, ρ_{00}) are related to the Stokes' parameters (P_1, P_2, P_3, P_4) through the following:

$$P_{lin}^{+}\, e^{2i\gamma} = P_1 + i\, P_2 \tag{2-3-5}$$

$$\rho_{00} = \frac{(1+P_1)(1-P_4)}{4-(1-P_1)(1-P_4)} \tag{2-3-6}$$

$$L_\perp = -P_3(1-\rho_{00}) \tag{2-3-7}$$

The characteristic lengths of the charge cloud are given by

$$l = (1-\rho_{00})\,\frac{1}{2}\,(1+P_{lin}^{+}) \tag{2-3-8.1}$$

$$w = (1-\rho_{00})\,\frac{1}{2}\,(1-P_{lin}^{+}) \tag{2-3-8.2}$$

$$h = \rho_{00} \tag{2-3-8.3}$$

with the condition $h + w + h = 1$.

It is often convenient to use the Blum-da Paixao parameters (λ, ε, $\bar{x}$, Δ) which are related to the Stokes' parameters by

$$\rho = -\frac{1}{2}\,(1-\lambda)(1-\cos\varepsilon) \tag{2-3-9.1}$$

$$P_1 = \frac{1}{2}\,[\lambda(3+\cos\varepsilon) - (1+\cos\varepsilon)] / (1-\rho_{00}) \tag{2-3-9.2}$$

$$P_2 = -2\sqrt{\lambda(1-\lambda)}\,\cos\bar{x} / (1-\rho_{00}) \tag{2-3-9.3}$$

$$P_3 = 2\sqrt{\lambda(1-\lambda)}\,\cos\Delta\,\sin\bar{x} / (1-\rho_{00}) \tag{2-3-9.4}$$

Chapter 3 Theoretical Details

§3.1 Basic Concepts

The principle of an electron-polarized-photon correlation experiment for the excitation of a heavy noble gas atom by electron impact can be written as

$$\text{Atom}\,(\,^1S_0\,) + e^- \rightarrow \text{Atom}^*(\,ns[3/2]^0_1 \text{ or } n's[1/2]^0_1\,) + e^{-\prime}$$

$$\downarrow$$

$$\text{Atom}\,(\,^1S_0\,) + \gamma$$

with $n = 3$ for Ne, $n = 4$ for Ar, and $n = 5$ for Kr when only the first excited states are studied.

For the excited states of the heavy noble gases, the influence of the spin-orbit interaction of the target electrons can no longer be neglected, so that the L-S coupling scheme is no longer valid. An intermediate angular momentum coupling scheme [Sobelman 1979] has to be used to characterize the excited state energy levels. Nonetheless, the traditional L-S coupling terminology is still used frequently in place of the more appropriate Racah notation. The spin-orbit-coupled excited states are often expressed in terms of L-S coupled states:

$$\text{"}^1P_1\text{"} = n's[1/2]^0_1 = a\,|^1P_1) + b\,|^3P_1)$$

$$\text{"}^3P_1\text{"} = ns[3/2]^0_1 = -b\,|^1P_1) + a\,|^3P_1)$$

with $a^2 + b^2 = 1$.

The mixing coefficients a and b for the heavy noble gases, which are known from atomic structure calculations and related experiments, are listed in table 3.1.1 together with the respective life-times of the excited states.

Table 3.1.1: The configuration coefficient of "$^1P_1$" and "$^3P_1$" and their lifetime on Neon, Argon and Krypton

	a	b	lifetime of "$^1P_1$" (ns)	lifetime of "$^3P_1$" (ns)
Neon n=3	0.964	0.266	1.8	32
Argon n=4	0.893	0.450	2.0	8.4
Krypton n=5	-0.683	0.730	3.11	3.18

The mixing coefficients are from Andersen et al. (1988), and the lifetimes are from Andersen et al. (1988) for neon, from the AIP Handbook of Physics (1982) for argon and from Matthias et al. (1977) for krypton.

The mixing coefficients indicate that the excited "$^1P_1$" and "$^3P_1$" states in Ne and Ar are preferentially of singlet and triplet character, respectively, whereas the distinction between singlet and triplet states is essentially meaningless in Kr and Xe [Martus et al. 1991, Becker et al. 1992].

The typical collision time ($\sim 10^{-15}$ sec) is much shorter than the time that characterizes the spin-orbit relaxation ($\sim 10^{-12}$ sec), the time of the Lamor precession of the electron spin ($\sim 10^{-12}$ sec), and the lifetime of the excited state of atom ($\sim 10^{-9}$ sec). Therefore, the collision process can be considered instantaneous. On the other hand, in comparison to the spin-orbit interaction time and the time of the Lamor precession of the electron spin, the lifetime of an excited state is long enough to cause the atom to relax completely into fine structure (and, where applicable, hyperfine structure) states, which, in turn, causes a depolarization of the emitted light in the subsequent decay process [Percival and Seaton 1958]. Since the spin-orbit interaction plays its important role in the collision, the positive reflection symmetry of the atomic charge cloud of the excited state with respect to the scattering plane can no longer be preserved.

While fine structure of the excited states is resolved in our experiment, the hyperfine structure of excited Kr (or Xe) states is not resolved and causes a partial depolarization of the subsequently emitted light. The only target that is affected by such hyperfine structure depolarization in this work is Kr, since natural Ne and Ar consist only of isotopes with nuclear spin $I = 0$ and no measurements were carried out in Xe. The partial depolarization of the measured polarization correlation parameters in Kr due to hyperfine structure depolarization has been calculated by Corr et al. [1991]. The effects are small, typically 4-6%.

The loss of atomic reflection symmetry is expressed by the "height" parameter ρ_{00}, which gives the relative probability of a spin flip perpendicular to the scattering plane. The non-zero value of ρ_{00} can, in fact, be due to two experimentally indistinguishable mechanisms, spin-orbit interaction and electron exchange.

There is a second independent process which connects the initial state of our experiment (incident electron + noble gas atom in the ground state) with the final state (scattered electron + noble gas atom in the ground state + photon). This process is the production of Bremsstrahlung by the incoming electron in the field of the atomic nucleus. Schematically we have

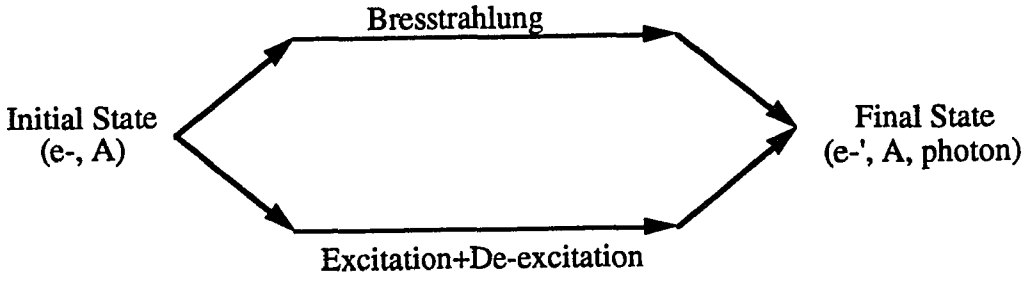

The Bremsstrahlung is continuous, so there is a finite probability for a Bremsstrahlung photon to have the same wavelength as the resonance photon from the decay of the excited noble gas atom. Therefore, both channels in the above diagram can in general occur. These two processes are experimentally indistinguishable and can interfere. However, the cross section ratio of the Bremsstrahlung channel to the electron impact excitation is less than 10^{-6} [Kim and Pratt 1986], so that the influence of the Bremsstrahlung channel on our experiment can be ignored.

It is useful to discuss briefly the simplest case of an atomic excitation by electron impact, the fully coherent excitation of the He n^1P_1 states from the 1^1S_0 ground state:

$$\text{He}\ (\ 1^1S_0\ ) + e- \rightarrow \text{He}\ (\ 2^1P_1\ ) + e'-$$

$$\downarrow$$

$$\text{He}\ (\ 1^1S_0\ ) + \gamma$$

In this process, the electron spin is a mere spectator and positive reflection symmetry with respect to the scattering plane is preserved. The most simplified theoretical approach to describe that process is a plane wave First-Born-Approximation (FBA) [Andersen et al. 1988]. The scattering amplitude in that case can be written as

$$f_{ba} = (\psi_b |\, e^{i\Delta\vec{k}\,\vec{r}} |\, \psi_a) \tag{3-1-1}$$

where $\Delta\vec{k} = \vec{k}_{in} - \vec{k}_{out}$ and ψ_a, ψ_b are the initial and the final state, respectively. ψ_a is a S-state wave function and ψ_b is a P-state wave function. We obtain:

$$L_\perp{}^{FBA} = 0 \tag{3-1-2}$$

$$P_{lin}^{+FBA} = 1 \tag{3-1-3}$$

$$\tan\gamma^{FBA} = \frac{\sin\Theta_e}{(\ \cos\Theta_e - x\ )} \tag{3-1-4}$$

with $x = \sqrt{\dfrac{E}{E - \Delta E}}$. Moreover, $P_4 = 1$ because of the atomic reflection symmetry.

As one might expect for a comparative simple theory such as the FBA, the agreement between experimental results and FBA predictions is generally poor. In He at intermediate impact energies (50 - 80 eV), experimental data start to deviate significantly from the FBA constraints for $L_\perp$ and P_{lin}^{+} (equation (3-1-2) and equation (3-

1-3)) at electron scattering angles around 40°. The same is true for the alignment angle γ. The FBA, in other words, provides an adequate description of the collision process only in the regime of very large impact parameters. For the heavy noble gases, equations (3-1-2) and (3-1-3) remain valid as does equation (3-1-4), albeit with appropriately modified parameters χ. Acceptable agreement between experimental data and the FBA predictions in the heavy noble gases was found to be restricted to even larger impact parameters (or smaller scattering angles) as will be discussed in more detail later.

So far, theoretical predictions for coherence parameters for heavy noble gas excitation have been obtained by two first-order perturbation approaches, the Distorted-Wave-Born-Approximation (DWBA) [Bartschat and Madison 1987], and the First-Order-Many-Body-Theory (FOMBT) [Thomas et al. 1974, Machado et al. 1982, 1984, 1991, da Paixao et al. 1984, Meneses et al. 1985, 1991]. In addition, a Relativistic-Distorted-Wave (RDW) calculation [Zuo et al. 1991], which is also a first-order perturbation approach, was carried out recently. The outline of the two main theoretical approaches, the DWBA and the FOMBT, will be presented in the following section. Generality will be preserved as much as possible.

The Hamiltonian of a electron-atom collision system consists of the kinetic energy of the electrons, the electron-nucleus interaction, and the electron-electron interaction. The electron-nucleus interaction includes the Coulomb potential $V_0 = -\frac{Ze^2}{4\pi\varepsilon_0 r}$, the spin-orbit interaction $H_2' = \frac{1}{2m^2c^2}\frac{1}{r}\frac{dV_0}{dr}\,\mathbf{L}\cdot\mathbf{S}$, a relativistic correction to the kinetic energy $H_1' = -\frac{p^4}{8m^3c^2}$, the Darwin term $H_3' = \frac{2\pi^3\hbar^2}{m^2c^2}\left(\frac{2e^2}{4\pi\varepsilon_0}\right)\delta(\mathbf{r})$, and the interaction between the nuclear spin and the

electron spin which causes the hyperfine structure $H_{hyper} = C\ \mathbf{I}\cdot\mathbf{J}$ [Bransden and Joachain 1983]. The electron-electron interaction includes the potential Coulomb interaction.

Before we discuss further details of the theoretical description of an electron-atom collision process, it is necessary to review the description of polarized light emitted by an electron-impact excited atom.

§3.2 The Polarization of the Emitted Light

Since the initial state and the final state of the atoms involved in the process that we study in our experiment are the same, namely, the $(np^6)\ ^1S_0$ ground state, the excited P-state, which can be expressed as a superposition of the magnetic sub-levels $|m_z\rangle$ with $m_z = 0, \pm 1$, contains the complete dynamical information of the excitation process (differential cross section as well as coherence parameters).

The following description follows the concept outlined in the paper of Fano and Macek [1973].

The intensity I of polarized emitted light in dipole transition can be written as

$$I = C \sum_{m_f} < |(f|\,\varepsilon^* \cdot \mathbf{r}|\,i)|^2 > \qquad (3\text{-}2\text{-}1)$$

where ε is the complex polarization (unit) vector, **er** is the electrical dipole moment. $|f\rangle$ is the final state and $|i\rangle$ is the initial state. The final state in our experiment is always the $^1S_0$ ground state. Possible initial states include all states with $J = 1$.

The constant C in equation (3-2-1) is given by:

$$C = \frac{e^2 \omega_{fi}^4}{2\pi c^3 R^2} \qquad (3\text{-}2\text{-}2)$$

with **R** is the distance vector from the source atom to the detector, and ω_{fi} is the angular frequency.

$< >$ denotes the average over the initial states and $\sum_{m_f}$ denotes the sum over the final states. Both the average and the sum depend on the specific situation in the experiment. Averaging and summing will cause a depolarization of the emitted light.

Blum [1981] introduced the concept of the "reduced density matrix" to incorporate the process of averaging and summing over unobserved parameters.

We re-write the intensity of the emitted light as:

$$I = C < \sum_{m_f} (i|\varepsilon\, \mathbf{r}|f)\bullet (f|\varepsilon^*\, \mathbf{r}|i) > \qquad (2\text{-}2\text{-}3)$$

If only the dipole operator variables $\mathbf{r}$ and $\mathbf{r}'$ are left unintegrated, we have

$$I = C < (i|\ \varepsilon\mathbf{r}'\bullet P_{f(\mathbf{r}',\,\mathbf{r})}\bullet\varepsilon^*\mathbf{r}\ |i) > \qquad (3\text{-}2\text{-}4)$$

The function $P_{f(\mathbf{r}',\,\mathbf{r})}$ is extracted after the integration.

We introduce the "detector frame" (ξ, η, ζ), a coordinate system, where $\hat{\xi} = \hat{R}$ is the unit vector from the source atom to the detector, $\hat{\zeta}$ is the arbitrary polarization unit vector in the plane perpendicular to $\hat{\xi}$, and $\hat{\eta} = \hat{\zeta} \times \hat{\xi}$ also lies in that plane. We can define

$$\varepsilon \equiv (\cos\beta,\ i\ \sin\beta,\ 0\ ) \equiv \hat{\zeta}\cos\beta + \hat{\eta}\ \sin\beta \qquad (3\text{-}2\text{-}5)$$

where $\beta = 0$ represents a linear polarization in the direction of $\hat{\xi}$, and $\beta = \frac{\pi}{2}$ represents a linear polarization in the direction of $\hat{\eta}$. $\beta = \frac{\pi}{4}$ represents right-handed circular polarization and $\beta = -\frac{\pi}{4}$ represents left-handed circular polarization.

In the established detector frame, we have

$$\varepsilon\mathbf{r}'\bullet\varepsilon^*\mathbf{r} = \xi'\xi\cos2\beta + \eta'\eta\sin2\beta - i\ (\xi'\eta - \xi\eta')\ \sin\beta\cos\beta \qquad (3\text{-}2\text{-}6)$$

which can be inserted into the intensity expression (3-2-4), to yield:

$$I = \frac{1}{3}\ C\ \{< (i|\ \mathbf{r}'\mathbf{r}\bullet P_{f(\mathbf{r}',\,\mathbf{r})}\ |i) >$$

$$- \frac{1}{2} < (i \mid (3\xi'\xi - \mathbf{r}'\mathbf{r}) \cdot P_{f(\mathbf{r}', \mathbf{r})} \mid i) >$$

$$+ \frac{3}{2} < (i \mid (\xi'\eta - \xi\eta') \cdot P_{f(\mathbf{r}', \mathbf{r})} \mid i) > \cos 2\beta$$

$$+ \frac{3}{2} < (i \mid i^{-1}(\mathbf{r}' \times \mathbf{r}) \cdot P_{f(\mathbf{r}', \mathbf{r})} \mid i) > \sin 2\beta \; \} \qquad (3\text{-}3\text{-}7)$$

which can be expressed as:

$$I = \frac{1}{3} C \; \{ < (i \mid S_0^{[0]} \mid i) >$$

$$- \frac{1}{2} < (i \mid S_0^{[2]} \mid i) >$$

$$+ \frac{3}{2} < (i \mid S_{2+}^{[2]} \mid i) > \cos 2\beta$$

$$+ \frac{3}{2} < (i \mid S_0^{[1]} \mid i) > \sin 2\beta \; \} \qquad (3\text{-}2\text{-}8)$$

Here $S_q^{[k]}$ defines the q-component of an irreducible tensor operator of rank k. The Wigner-Eckart theorem [Lichtenberg 1978] states that the ratio of the matrix elements $(i \mid S_q^{[k]} \mid i)$ and $(i \mid T_q^{[k]} \mid i)$ is independent of the magnetic quantum numbers, m_i , $m_{i'}$ and of q. Let $T_q^{[k]}$ be another component of an arbitrary irreducible tensor operator of the same rank. Then:

$$< (i \mid S_q^{[k]} \mid i) > = < (i \mid T_q^{[k]} \mid i) > \cdot \frac{< i \mid S_q^{[k]} \mid i) >}{(i \mid T_q^{[k]} \mid i) >}$$

$$= < (i \mid T_q^{[k]} \mid i) > \cdot \frac{(i \mid\mid S^{[k]} \mid\mid i)}{(i \mid\mid T^{[k]} \mid\mid i)} \qquad (3\text{-}2\text{-}9)$$

The second term in the above equation represents the ratio of the so-called "reduced matrix" [Blum 1981], which is independent of q, m_i and $m_{i'}$.

It is obvious that the construction of the irreducible tensor operator $T_q^{[k]}$ in terms of products of angular momentum components J_ξ, J_η and J_ζ will lead to a direct and convenient formulation for the polarization of the emitted light. We choose $T_q^{[k]}$ through the mapping the $\mathbf{r}$ to $\mathbf{J}$ without $P_{f(\mathbf{r}', \mathbf{r})}$

$$T_0^{[0]} = \mathbf{J}^2 \tag{3-2-10.1}$$

$$T_0^{[2]} = 3J_\xi^2 - \mathbf{J}^2 \tag{3-2-10.2}$$

$$T_{2+}^{[2]} = J_\xi^2 - J_\eta^2 \tag{3-2-10.3}$$

$$T_0^{[1]} = i^{-1}(\mathbf{J}\times\mathbf{J})_\zeta = J_\zeta \tag{3-2-10.4}$$

With these definitions, the ratio of k-th reduced matrix elements in (3-2-9) can be simplified as the ratio of scalar elements (zeroth order) multiplied by a number, which is composed of 6j-coefficients [Edmonds 1957, Fano and Racah 1959]. Specifically, we have

$$\frac{(i\|S^{[k]}\|i)}{(i\|T^{[k]}\|i)} = h^{(k)}(j_i, j_f)\cdot\frac{(i\|S^{[0]}\|i)}{(i\|T^{[0]}\|i)} \tag{3-2-11}$$

with

$$\frac{(i\|S^{[0]}\|i)}{(i\|T^{[0]}\|i)} = \frac{(i\|S^{[0]}\|i)}{j_i(j_i+1)}$$

The value of $h^{(k)}(j_i,j_f)$ is defined by 6j-coefficients [Rotenberg et al. 1959]:

$$h^{(k)}(j_i, j_f) = (-1)^{j_i-j_f}\ \frac{\begin{bmatrix} j_i & j_f & k \\ 1 & 1 & j_f \end{bmatrix}}{\begin{bmatrix} j_i & j_f & k \\ 1 & 1 & j_i \end{bmatrix}} \tag{3-2-13}$$

We note that

$$(i||S^{[0]}||i) = S \tag{3-2-14}$$

We obtain

$$I = \frac{1}{3}CS\ \{\,1 - \frac{1}{2}h^{(2)}(j_i, j_f) < (i|3J_\xi^2 - \mathbf{J}^2|i) > / j_i(j_i+1)$$

$$+ \frac{3}{2}h^{2}(j_i, j_f) < (i|J_\xi^2 - J_\zeta^2|i) > / j_i(j_i+1)\ \cos 2\beta$$

$$+ \frac{3}{2}h^{(1)}(j_i, j_f) < (i|J_\zeta|i) > / j_i(j_i+1)\ \sin 2\beta\ \} \tag{3-2-14}$$

Two alignment parameters can be defined as follows:

$$A_0^{\det} = < (i|3J_\xi^2 - \mathbf{J}^2|i) > / j_i(j_i+1) \tag{3-2-15.1}$$

$$A_{2+}^{\det} = < (i|J_\xi^2 - J_\eta^2|i) > / j_i(j_i+1) \tag{3-2-15.2}$$

and an orientation parameter can be introduced through:

$$O_0^{\det} = < (i|J_\zeta|i) > / j_i(j_i+1) \tag{3-2-15.3}$$

Therefore, the intensity of the polarized light I can written as

$$I = \frac{1}{3}CS\ \{\,1 - \frac{1}{2}h^{(2)}(j_i, j_f)\bullet A_0^{\det}$$

$$+ \frac{3}{2}h^{(2)}(j_i, j_f)\bullet A_{2+}^{\det}\ \cos 2\beta + \frac{3}{2}h^{(1)}(j_i, j_f)\bullet O_0^{\det}\ \sin 2\beta\ \} \tag{3-2-16}$$

In the case of $\beta = 0$ or $\beta = \frac{\pi}{2}$, the alignment parameter $A_{2+}^{\det}$ is responsible for part of the linear polarization, and in the case of $\beta = \pm\frac{\pi}{4}$, the orientation parameter $O_0^{\det}$ produces part of the circular polarization. So far, the alignment and orientation parameters still depend on the location and orientation of the detector frame (ξ, η, ζ), so that further simplifications are necessary to obtain frame-independent alignment.

and orientation parameters.

When we apply the above formulas to our electron-polarized photon coincidence experiment, we may select the collision frame as a possible reference frame. The collision frame has the direction of the incident electron beam as its axis of quantization. In that case, the relation between the detector frame and the collision frame is given by

θ = *angle between* ζ and z^c

ψ = *angle between* ξ and *plane* (ζz^c)

ϕ = *angle between plane* $(z^c x^c)$ and *plane* (ζz^c)

The standard alignment and orientation parameters in the collision frame (x^c, y^c, z^c) are introduced as follows:

The alignment parameters

$$A_0^{col} = < (i \,|\, 3J_z^2 - \mathbf{J}^2 \,|\, i) > / j_i(j_i+1) \qquad (3\text{-}2\text{-}17.1)$$

$$A_{2+}^{col} = < (i \,|\, J_x^2 - J_y^2 \,|\, i) > / j_i(j_i+1) \qquad (3\text{-}2\text{-}17.2)$$

$$A_{1+}^{col} = < (i \,|\, J_x J_y + J_y J_x \,|\, i) > / j_i(j_i+1) \qquad (3\text{-}2\text{-}17.3)$$

and the orientation parameter

$$O_0^{col} = < (i \,|\, J_z \,|\, i) > / j_i(j_i+1) \qquad (3\text{-}2\text{-}17.4)$$

The relation of the two sets of alignment and orientation parameters in the two frames can be derived through transformation of the angular momentum operators from one frame into the other:

$$A_0^{\det} = A_0^{col} \frac{1}{2}(3\cos^2\theta - 1) + A_{1+}^{col} \frac{3}{2}\sin 2\theta \cos\phi$$

$$+ A_{2+}^{col} \frac{3}{2}\sin^2\theta\cos2\phi \qquad (3\text{-}2\text{-}18.1)$$

$$A_{2+}^{det} = A_0^{col} \frac{1}{2}\sin^2\theta\cos2\psi + A_{1+}^{col} [\ \sin\theta\cos\phi\sin2\psi + \sin\theta\cos\theta\sin\phi\cos2\psi\ ]$$

$$+ A_{2+}^{col} [\ \frac{1}{2}(1+\cos^2\theta)\cos2\phi\cos\psi - \cos\theta\sin2\phi\sin2\psi\ ] \qquad (3\text{-}2\text{-}18.2)$$

$$O_0^{det} = O_{-1}^{col} \sin\theta\cos\phi \qquad (3\text{-}2\text{-}18.3)$$

Up to now, the intensity of the emitted polarized light has been expanded in terms of the three alignment parameters A_0^{col}, A_{1+}^{col}, A_{2+}^{col} and the orientation parameter O_{1-}^{col} with the collision frame as the reference frame.

It is interesting to discuss the special case of an electron-polarized photon coincidence experiment in the forward scattering direction (Θ_e=0). In this case, we have $A_{2+}^{col} = 0$ because of the cylindrical symmetry about the z^c-axis (incident electron beam). During the collision linear momentum is transferred only along the z^c-axis, so that no orbital angular momentum can be transferred in the z^c direction. If the initial atomic state before the excitation is a singlet S-state ($^1S_0$), as in our experiment, we have

$$< (i\,|\, J_z^2 \,|\, i) > = 0$$

after the collision, which leads to $A_{1+}^{col} = 0$, $O_{1-}^{col} = 0$, and $A_0^{col} = -1$. The ϕ independence due to the cylindrical symmetry about the z^c-axis, leads to $A_{1+}^{col} = 0$ and $O_{1-}^{col} = 0$. When $\beta = 0$, the light intensity becomes

$$I = CS\ \sin^2\theta\ [\frac{1}{2}(1 + \cos2\psi)] \qquad (3\text{-}2\text{-}19)$$

which means the emitted light is completely linearly polarized, $P_1 = 1$, along z^c.

We frequently used the non-coincident radiation pattern in He at 50eV or 40eV to calibrate the optically flat, gold-coated mirror used for the VUV polarization analysis. This situation is also characterized by a cylindrically symmetric collision process, so that the same formulation can be applied:

$$A_0^{\text{det}} = A_0^{col} \frac{1}{2}(3\cos^2\theta - 1) \tag{3-2-20.1}$$

$$A_{2+}^{\text{det}} = A_0^{col} \frac{1}{2}\sin^2\theta\cos 2\psi \tag{3-2-20.2}$$

and

$$O_0^{\text{det}} = 0 \tag{3-2-20.3}$$

$O_0^{\text{det}} = 0$ reveals that the non-coincident radiation pattern does not provide any information about the circular polarization as expected.

When the above formulation is applied to a case where the spin-orbit interaction is present, it is convenient to introduce a different (although equivalent) set of coherence parameters, the Blum-da Paixao parameters:

$$A_0^{col} = \frac{1}{2}(1-3\lambda) \tag{3-2-21.1}$$

$$A_{1+}^{col} = [\lambda(1-\lambda)]^{1/2} \cos\bar{\chi} \cos\Delta \tag{3-2-21.2}$$

$$A_{2+}^{col} = \frac{1}{2}(\lambda-1) \cos\varepsilon \tag{3-2-21.3}$$

and

$$O_{1-}^{col} = -[\lambda(1-\lambda)]^{1/2} \sin\bar{\chi}\cos\Delta \tag{3-2-21.4}$$

§3.3 The Distorted Wave Born Approximation (DWBA)

The distorted wave approach in scattering theory is a well-established technique [Mott and Massey 1987, Bransden and McDowell 1977, Vanderpoorten and Winters 1979, Walters 1984]. The basic idea of the distorted wave method is to split the interaction term in the Hamiltonian into two parts U and W, so that the Hamiltonian has the form $H = K + U + W$, where K is the kinetic energy and U is the interaction potential. The Hamiltonian $H_0 = K + U$ can be solved either analytically or numerically. At the same time, the perturbation term W is chosen in such way that the convergence of perturbation expansion is optimized.

Formal scattering theory [Goldberger and Watson 1964] is employed to describe the collision process and to determine the wave functions, the S-matrix, and the T-matrix.

The incoming and outgoing wave functions of the initial state and the final state are written as

$$\psi_i^+ = \chi_i + \frac{1}{E_i - H + i\eta}(H - E_i)\chi_i \qquad (3\text{-}3\text{-}1.1)$$

$$\psi_f^- = \chi_f + \frac{1}{E_f - H - i\eta}(H - E_f)\chi_f \qquad (3\text{-}3\text{-}1.2)$$

where η is infinitesimal; χ_i, χ_f are the initial and the final non-interaction states; E_i, E_f are the initial and final energies of the collision system. The S-matrix is given by

$$S_{fi} = (\chi_f, \psi_i^+) \qquad (3\text{-}3\text{-}2.1)$$

S_{fi} can also be written as

$$S_{fi} = \delta_{fi} - 2\pi i\delta(E_f - E_i)\, T_{fi} \qquad (3\text{-}3\text{-}2.2)$$

with

$$T_{fi} = \left((H - E)\psi_f, \psi_i^+\right) \tag{3-3-2.3}$$

where we set $E_i = E_f = E$.

The configuration of the system before and after the collision may be different, so that the Hamiltonian of the system can be configured in different ways. In the case of our experiment, the interaction term $V = U + W$ is formed in different ways:

$$V = \begin{cases} U_i + W_i & \textit{for the initial state} \\ U_f + W_f & \textit{for the final state} \end{cases} \tag{3-3-3}$$

The U_i, U_f are the so-called distorting potentials for the initial and the final state, respectively. The principle reason to divide the interaction term V into two parts U and W is that the W term would be perturbated in highly effective way. To achieve that high effectiveness, the U term is should be chosen in such way that the collision system with Hamiltonian $H_0 = K + U$ can be solved either analytically or numerically and contributes no inelastical scattering, and at same time the V term should play a role of most of mean field in the interaction term V. More discussion will be presented later in this section.

The T-matrix has been written as

$$T_{fi} = \left(\chi_f, (U_f + W_f)\psi_i^+\right) = \left(\chi_f^-, W_f\psi_i^+\right) + \left(\chi_f^-, U_f\chi_i\right) \tag{3-3-4.1}$$

with

$$\chi_f^- = \chi_f + \frac{1}{E - K - i\eta} U_f\chi_f^- \tag{3-3-4.2}$$

$$\psi_i^+ = \chi_i^+ + \frac{1}{E - H + i\eta} W_i\chi_i^+ \tag{3-3-4.3}$$

along with

$$\chi_i^+ = \chi_i + \frac{1}{E - K + i\eta} U_i \chi_i \tag{3-3-4.4}$$

So, we can re-write the T-matrix as

$$T_{fi} = (\chi_f^-, U_f \chi_i) + (\chi_f^-, W_f \chi_i^+) + (\chi_f^-, W_f G^+ W_i \chi_i^+) \tag{3-3-5}$$

with the Green's function operator

$$G^+ = \frac{1}{E - H + i\eta} \tag{3-3-6.1}$$

The distorting potential U_i, U_f have to be chosen for the initial state and the final state, respectively. The remaining part of the interaction term is $W_i = V - U_i$, and $W_f = V - U_f$, respectively. The Green's function operator can be expanded in a perturbation series

$$G^+ = G_0^+ + \frac{1}{E - K - U + i\eta} W G^+ \tag{3-3-6.2}$$

with $G_0 = \frac{1}{E - K - U + i\eta}$ and $H = K + U + W$.

In the expression for the T-matrix (3-3-5), the three distorting potentials U_i, U_f and U can be chosen arbitrarily. In practice, the following conditions and considerations should be applied when choosing the distorting potentials:

(a) If the three distorting potentials are purely potential interactions, then the first term of the T-matrix expression (3-3-5) contributes only to the direct elastic scattering. The second term contributes to the first order and to the higher order direct amplitudes and exchange amplitude for both elastic and inelastic scattering. The third term contributes to the second order and to the higher order direct

amplitudes and exchange amplitudes for both elastic and inelastic scattering.

(b) Up to now, only first-order calculations have been carried out for heavy noble gas excitation. So, the following discussion is restricted to the first order approximation.

(c) The distorting potentials U_i and U_f are chosen in such way that the Hamiltonian $H_0 = K + U_i$ or $H_0 = K + U_f$ can be solved either analytically or numerically

(d) The distorting potentials U_i and U_f are also chosen from the point of view of maximizing the rate of convergence of the perturbation expansion. In other words, the distorting potentials play a role similar to that of the mean field in the interaction term in the Hamiltonian.

One of the most important points in the DWBA is how to choose the initial and final state distorting potentials. Intuitively, one would expect that the incoming electron should be distorted by the initial state of the atom and that the outgoing electron should be distorted by the final state of the atom. This type of calculation is called DWB1-MM with MM referring to the Mott and Massey's consideration [1987]. However, this intuitive choice for the distorting potential typically produces results which are not in very good agreement with experimental differential cross section measurements. The distorted wave model may also be developed from the First-Order-Many-Body Theory [Thomas et al. 1987, Cartwright and Csanak 1987], and in this approach, it is required that both U_i and U_f be chosen as the initial ground state potential. While such a choice is not as intuitively appealing, it can be regarded as a model in which an excitation process happens after the electron passes the atom, so that the projectile electron is predominantly in the field of the ground state.

Significantly better agreement with experimental differential cross sections is obtained by using a model in which both the incoming and the outgoing electrons are distorted by the final atomic state, that is, the excitation process takes place early in the collision (this model is called DWB-EP). Similarly, Srivastava et al. [1989] noted that using $(U_i + U_f)/2$ to distort both the incoming and the outgoing electron also yields reasonably good agreement with experiment for excitation of the 2^1P state of He. Several attempts have been made to provide a satisfactory theoretical justification for these types of models, but none has been found. The success, particularly of the DWB1-EP model for different atoms, energies, and atomic transitions, indicates that it contains some important physics that is yet to be explained.

§3.4 The First Order Many Body Theory (FOMBT)

The essential motivation for the First-Order-Many-Body-Theory (FOMBT) approach [Schneider et al 1970, Csanak et al 1971a, 1971b, Csanak et al 1973] is to create an approach of a non-perturbative and self-consistent approximation from the Green's function technique which is different from the approach of a perturbative method such as the DWBA. The basic idea of the FOMBT was initially developed by Schneider, Taylor and Yaris [1970]. The many-body Green's function techniques of Martin and Schwinger [1959] was employed by these authors to the case of elastic scattering of electrons from atoms in an attempt to develop an approach, in which a "linear response" approximation was introduced and combined with a self-consistent method. The subsequent paper by Csanak, Taylor and Yaris [1971a] applied that same approach to the case of inelastic scattering of electrons from atoms and from ions.

Theoretical predictions from the FOMBT have so far been obtained for excitation of the n's$[1/2]^0_1$ and ns$[3/2]^0_1$ states of Ne, Ar and Kr [Machado et al 1981, 1982, da Paixao et al 1984, Meneses et al 1985, 1991, Csanak and Meneses 1991].

The basic concepts of the FOMBT have been presented in the review paper [Csanak, Taylor and Yaris 1971b].

Chapter 4 Experimental Details

The experimental requirements to carry out the proposed electron-photon coincidence experiments with a polarization analysis of the vacuum ultraviolet (VUV) rare gas resonance radiation can be summarized as follows:

(1) a vacuum chamber with a base pressure of 1×10^{-7} Torr without target gas beam and about 7×10^{-7} Torr under operating conditions (i.e. with the gas beam on)

(2) a well-defined electron beam of variable energy (20 - 120 eV), variable current (5 - 100 nA), and variable energy resolution (100 - 250 meV).

(3) a spatially well-defined gas beam with a number density of up to 5×10^{10} atoms/cm^3 in the interaction region.

(4) a rotatable electron analyzer (-20° to +90°) with an energy resolution of 100-250 meV (for the combined monochromator-analyzer system).

(5) a detector suitable for the detection and the polarization analysis of photons in the VUV below a wavelength of 130 nm.

(6) fast pulse counting electronics that allows the correlated detection of scattered electrons and decay photons with nanosecond time resolution.

(7) the capability to acquire electron-photon coincidence data over periods of days and to transfer the data to a computer for permanent storage and further analysis.

A schematic diagram of the experimental apparatus was presented in figure 2.1.1. Details of the various components and of their performance characteristics will be given in the following sections. It should be noted that a very detailed apparatus description has been given in a previous thesis [Martus 1990]. Therefore,

experimental details in this thesis will be kept to a minimum. Detailed discussions will be limited to new experimental developments that are unique to the work presented in this thesis.

§4.1 The Vacuum System

The experiment is housed in a cylindrically shaped stainless steel vacuum chamber with an inner diameter of 12″ and a height of 11″. The chamber has ten ports located on the cylindrical wall. Theses ports are utilized as (1) a rotary motion feedthrough to rotate the electron analyzer; (2) a nine-pin electrical feedthrough for the electron analyzer and connections for the electron gun filament current; (3) a two-pin high-voltage electrical feedthrough for the connections of the electron detector; (4) a gas inlet flange; (5) a nine-pin electrical feedthrough for the electron monochromator connections; (6) a four-pin electrical feedthrough for an internal baking lamp; (7) an ionization gauge; and (8) three blank flanges.

There are three 2″ diameter port holes on the top flange. These are used for (1) a four-pin high-voltage electrical feedthrough for the photon detector; (2) a rotary motion feedthrough for the VUV polarization analyzer; and (3) an eight-pin electrical feedthrough for an in-vacuum stepper motor, which is used for the circular polarization measurements only.

The vacuum chamber is evacuated through a 6.0″ diameter hole in the bottom plate. A Sargent Welsh model 3133C turbomolecular pump with a nominal pumping speed of 600 *l/s* backed by a Sargent Welsh model 8851 direct-drive roughing pump achieves ultimate base pressures of about 1×10^{-7} Torr or slightly below in the vacuum chamber. The vacuum is monitored using a Bayard-Alpert type ionization gauge (Granville Phillips model 274003) connected to a Granville Phillips model 260 ionization gauge controller. Base pressures of about 3×10^{-7} Torr could be achieved after only 36 hours of pumping without any bake-out.

The magnetic field inside the vacuum chamber is reduced to less than 10 mG in the interaction region of the electron beam and the gas beam by a single sheet of μ-metal (3/4 mm thickness) placed inside the chamber. In addition, the electron monochromator and the analyzer are housed in separate μ-metal boxes to reduce the magnetic field along the electron beam path even further. The residual magnetic field of the stainless parts inside the μ-metal shield was reduced by de-magnetizing all parts that were used for the assembly of the apparatus.

§4.2 The Electron Spectrometer

A commercially available spectrometer, Comstock model AC-901, was used to produce the incident electron beam and to analyze the scattered electrons. The spectrometer, which was slightly modified [Martus 1990], consists of an electrostatic electron monochromator and a similar electrostatic electron analyzer. The monochromator consists of an electron gun as an electron source, a 160° double-focusing spherical electrostatic analyzer to reduce the energy spread of the electron beam, and a three-element Einzel lens to focus the electron beam into the interaction region. The rotatable analyzer has an identical input Einzel lens to focus the scattered electrons onto the entrance aperture of a similar electrostatic analyzer and an electron detector to detect those electrons that have been scattered into a particular angle and that have lost a specific amount of kinetic energy.

A schematic diagram of spectrometer was shown in figure 2.2.1, figure 2.2.2 and figure 2.2.3. Additional details can be found in the thesis of Martus [1990].

The monochromator assembly is mounted on an aluminum stand which allows a two-dimensional alignment of the position of the incident electron beam. A teflon spacer insulates the monochromator from the aluminum stand. The entire assembly is shielded by a μ-metal box to reduce the magnetic field inside the monochromator further.

The electron analyzer is mounted on a Plexiglass base and is enclosed in a separate μ-metal box. The box is mounted on a plate that can be rotated about the center of the interaction region. The box can be shifted horizontally relative to the mounting plate and can also be adjusted vertically. The rotation of the analyzer is

achieved by a rotary motion feedthrough and a set of bevel gears from outside the vacuum chamber. The range of scattering angles that can be covered with the present arrangement encompasses -20° to +90°.

The electron analyzer consists of an input Einzel lens similar to the output lens of the electron monochromator (both lenses include an additional grounded lens element), another 160° double focusing spherical energy selector, and a channel-electron multiplier (CEM).

A Farady cup is mounted at the back of the energy selector of the analyzer for alignment purposes and to monitor the electron beam.

The energy selected electrons after passing through the selector are detected by a Galileo-Electro-Optics model 4093C Channeltron (CEM) located at the exit aperture of the analyzer. The Channeltron and its cables are shielded to avoid stray fields and electrical pickup.

The parts of the electron spectrometer that are exposed directly to the electron beam are coated with Aerodag-G, produced by Acheson Colloids Company. Aerodag-G is a colloidal graphite dissolved in isopropyl alcohol. A coating of Aerodag-G reduces the yield of elastically reflected electrons as well as the formation of secondary electrons [Kollath 1937, 1956, 1958], and it produces comparatively uniform surface potentials. This is especially important at energies below 30 eV. Small alignment holes were drilled in the back of both selectors. These two holes in conjunction with the monochromator exit aperture (AP2), the analyzer entrance aperture (AP3) and the tip of the gas nozzle were used to facilitate the mechanical alignment of the electron spectrometer using a HeNe laser beam. The carbon coating was found to deteriorate over time which, in turn, resulted in reduced performance

characteristics of the electron spectrometer. The deterioration occurred more quickly when high electron beam currents were employed. Typically, we had to dissemble the spectrometer and re-coat the parts after several weeks of the data acquisition.

§4.3 The Gas Beam

We used target gases neon, argon, and krypton of research grade quality supplied by Air Products and Chemicals Inc. with stated purities of 99.99%, 99.998%, and 99.995% for neon, argon and krypton, respectively. The gas handling system consists of a two stage pressure regulator (Air Products model E12-2-N515B), which reduces the cylinder pressure to about 700-1000 Torr. A teflon line connects the regulator to a Granville Philips Model #203 Variable Leak Valve which introduces the gas into the vacuum chamber. The pressure in the line to the nozzle is monitored by a MSK model 127AA-00010A Baratron pressure transducer connected to a MKS model PDR-C-C controlling unit. Typical driving pressures range from 0.30 to 0.45 Torr.

The gas line is connected to the vacuum chamber using two Swagelok connectors fastened anti-parallel to a stainless steel flange. The in-vacuum gas line is connected to the gas nozzle assembly through another Swagelok connector and flexible teflon tubing. The gas nozzle assembly consist of three vacuum compatible linear motion translators to position the gas nozzle. The nozzle is oriented at right angles to the incident electron beam. A single capillary injects the gas into the interaction region. The capillary has an inner diameter of about 0.2 mm and is 1 cm long.

A thermal molecular beam is typically produced by effusing molecules through a narrow capillary. Molecular flow conditions require

$a \ll \lambda$, a: radius of the capillary; λ: mean free path

$L < \lambda$, L: length of the capillary

Details regarding molecular beam formation can be found in the original papers of Knudsen (1909), Smoluchowski (1910), Clausing (1931), and Kennard (1938) and in the book by Ramsey (1956). In most models, it is assumed that molecules scatter isotopically off the walls of the capillary which is justified for most metal surfaces. As a consequence, the gas expands isothermally and the mean thermal energy of the gas molecules (i.e. the temperature) is determined by the temperature of the walls of the capillary. For typical head pressures of 0.1 - 1.0 Torr, most gases are described by the ideal gas law. Both the internal energy and the enthalpy are only functions of temperature. No work is done on the expanding gas, and the velocity distribution remains unchanged. Giordmaine and Wang (1960) gave a specific function for the beam intensity under the above conditions for a single capillary.

Our experimental system is operated at room temperature. The driving pressure in the gas line justifies the use of the ideal gas law for our experimental conditions. The mean free path λ which was estimated from the ideal gas law [Feynman 1963] for our experimental conditions is close to the radius of the capillary (0.2 mm) and thus violates the condition $L < \lambda$. Therefore, the functional form of the beam intensity given by Giordmaine and Wang (1960) is not applicable to our experimental conditions.

On the other hand, molecular beam conditions and a quantitative knowledge of the number density of gas molecules in the interaction are not crucial to our experiment. Therefore, we will not discuss the details of the gas beam properties any further other than giving an upper limit on the number densities used in our experiment, which is 5×10^{10} atoms/cm^3 based on a calculation for conditions where molecular flow conditions do no longer hold [Zuegenmaier 1966].

§4.4 Polarization Analysis in the VUV

There is no material that allows a linear and circular polarization analysis of photons below 125 nm based on transmission optics, which is the common technique in the visible and near ultraviolet. Instead, reflection optics has to be employed, which utilizes the difference in $\mathbf{R}_{\perp}$ and $\mathbf{R}_{\parallel}$, the reflectivity perpendicular and parallel to the plane of incidence, for polarization analysis purposes. The first compact and easy-to-use reflection-type VUV polarization analyzer for linear and circular polarization in the VUV was developed by McConkey and collaborators [Zetner et al. 1983, 1984, Westerveld et al. 1985]. The polarization analyzer uses either a single-reflection (for linear polarization analysis) or a double-reflection (for linear as well as for circular polarization analysis) from a flat gold surface.

In this section, we only focus on the measurements of the linear polarization in the VUV.

It can be shown that at an angle of incidence of 60° on an optically flat gold surface the component of the electric vector perpendicular to the plane of incidence is about five times more efficiently reflected than the parallel component for incident photons of wavelengths around 100 nm [Zetner et al. 1983, 1984]. This translates into a linear polarization sensitivity for a single reflection of roughly 66%. Additional reflections will cause the polarization sensitivity to increase rapidly to about 90%. However, each reflection also means a loss of intensity, so that the gain in polarization sensitivity from using multiple reflections is achieved at the expense of a reduced transmission. We used a single-reflection polarization analyzer for increased signal strength for all linear polarization measurements carried out as part of this

thesis. The photons emitted along the axis of the polarizer are reflected from the gold surface at an incidence angle of incidence of 60°. The reflected photons are detected by a channel electron multiplier (CEM, Galileo-Electro-Optics model 4093C Channeltron) mounted behind the exit aperture of the polarization analyzer. In addition, a negative bias voltage (about 200 V) was applied to the cone of CEM to repel any stray electrons. The high voltage and the bias voltage leads were shielded with wire mesh and with μ-metal foil.

The VUV wavelengths of relevance in our experiment are 73.59 nm (from the decay of the "$^1P_1$" state of Ne), 104.82 nm ("$^1P_1$" in Ar), and 116.49 nm ("$^1P_1$" in Kr) and 123.58 nm ("$^3P_1$" in Kr). For calibration purposes (as discussed later), we also employed the wavelength of 58.43 nm corresponding to the decay of the 2^1P_1 state in He.

An uncoated CEM is used for detecting the VUV photons of wavelengths shorter than 110 nm, and a cesium iodide coated CEM is used to detect the VUV photons of wavelengths longer than 110 nm. Absolute detection efficiencies of the CEM for the above wavelengths are about 5-10% depending on the wavelength, the high voltage applied to the CEM, and the pre-condition of the CEM. Even though the polarization analyzer detects photons of all wavelengths below its cut-off at about 150 nm, this does not affect the physics of our experiment, since we accomplish the state selection in the electron channel. The details of the coincidence experiment including electron detection and coincidence electronics will be presented in a later chapter.

In principle, all reflection properties can be calculated from the complex index of refraction ($n - i\,k$) of a material, gold in our experiment. The indices n and k

of gold have been determined experimentally and can be found in the book of Samson [1967], for example, for the wavelength range 20 - 200 nm. Gold is the material of choice because it has unique optical properties. (Details will be given in a later chapter. See also Zetner 1983, 1984, Samson 1967.)

Chapter 5 Experimental Procedure

§5.1 Operation of the Electron Spectrometer

The energy of the incident electron beam (20 - 120 eV) is essentially determined by the voltage difference between the filament tip (and housing) and the electrostatically grounded exit aperture of the electron monochromator, which is at the same potential as the interaction region. The proper voltages for the various spectrometer elements can in principle be calculated (e.g. Harting and Read 1976), but it was found more practical to determine the voltages empirically by monitoring the electron beam, the photon signal, and the electron energy loss spectrum.

The actual energy of the incident electron beam is slightly different from the externally applied voltage due to contact potentials. A contact potential occurs at a metal-metal interface and is due to a difference in the Fermi levels of the materials [Eisberg and Resnick 1985]. The effect of contact potentials and hence the calibration of the electron energy was determined experimentally by measuring the total yield of VUV photons in neon as a function of electron energy and comparing the positions of characteristic structures such as the onset or resonance structures to the well-established values of these features.

Figure 5.1.1 shows the total yield of VUV photons produced by electron impact on neon as a function of electron energy. Electrons with energies below the threshold for excitation of the VUV emitting levels (nominally at 16.67 eV) cannot excite the atoms and there is no subsequent VUV emission. The onset of the photon emission occurs when the incident electron energy is equal to the excitation threshold. The measured onset in comparison to the spectroscopic value of the onset provides one of

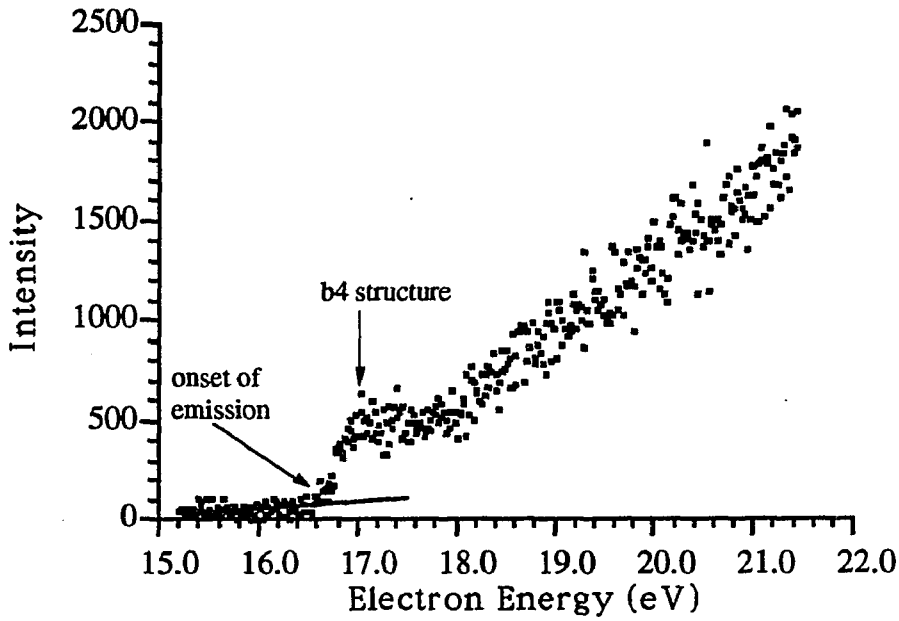

Figure 5.1.1: VUV photon yield as a function of incident electron energy in neon.

the benchmarks used to calibrate the electron energy. The onset in figure 5.1.1 is determined to be at 16.60 eV from the intercept of the background and the linear extrapolation of the photon yield curve. A comparison with the spectroscopic value of 16.67 eV yields a contact potential of -0.07 V. As a second independent check, we compared the position of the resonance structure, labeled "b4" in figure 5.1.1, which was identified in the high-resolution work of Brunt et al. [1977] to occur at 17.05 eV. This comparison yielded a contact potential of 0.01 V. The comparison with the resonance structure is more precise, since it does not depend on separating the background from the signal. Typically, contact potentials of a few tenths of an electron volt were found which could be determined to a precision of ±0.05 eV, and which were stable to within ±0.10 eV over periods of weeks.

The energy resolution of the electron spectrometer can be varied by changing the energy selector entrance and exit aperture sizes and by changing the transmission energy of the beam through the selectors. The energy spread of electrons produced by a heated tungsten filament is typically 0.5-0.8 eV (fwhm). The energy resolution of the incident electron beam is mainly determined by the spherical energy selector, and can be expressed in term of the ratio of ΔE/E [Moore et al. 1983]:

$$\frac{\Delta E}{E} = \frac{\omega}{R(1-\cos\theta) + l\sin\theta} \qquad (5\text{-}1\text{-}1)$$

where

ω is the diameter of the apertures AP1 and AP2,

R is the mean radius of the electron path in the selector (here 3.6 cm),

θ is the bending angle by the energy selector (here 160°)

l is the distance from exit aperture of the energy selector to the final exit aperture (here 1.07 cm)

E is the transmission energy

ΔE is the energy fwhm (full width of half maximum)

The energy resolution for the analyzer can be obtained by the same equation (5-1-1).

It is very convenient to use the same aperture size for AP1, AP2, AP3 and AP4 (see figure 2.2.2 and figure 2.2.3) and to employ also the same transmission energy in the monochromator and the analyzer. For equal transmission energies in the monochromator and the analyzer, the overall energy resolution of the electron spectrometer is $\sqrt{2}$ times the energy resolution of either the monochromator or the analyzer. The performance of the electron spectrometer was checked regularly by measuring the fwhm of an isolated peak in the krypton energy loss spectrum. Figure 5.1.2 shows a typical electron energy loss spectrum of krypton at an incident electron impact energy of 50 eV and a scattering angle of 7.5° with aperture sizes of 1.0 mm and a transmission energy of 15 eV. The first two peaks in figure 5.1.2 correspond to the excitation of respectively the "$^3P_1$" state at 10.04 eV and the "$^1P_1$" state at 10.64 eV. The fwhm of either peak indicates an overall energy resolution of the spectrometer of about 230 meV in good agreement with the calculated energy resolution for these spectrometer operating conditions.

The inelastic differential scattering cross section drops dramatically with increasing scattering angle in the region 0° - 50° for electron impact energies from 30 eV to 50 eV. Coincidence spectra with sufficient accuracy are typically obtained in ½ to 5 days depending on the scattering angle and the impact energy. Typical count rates in the electron channel range from 25 kHz close to the forward scattering direction to

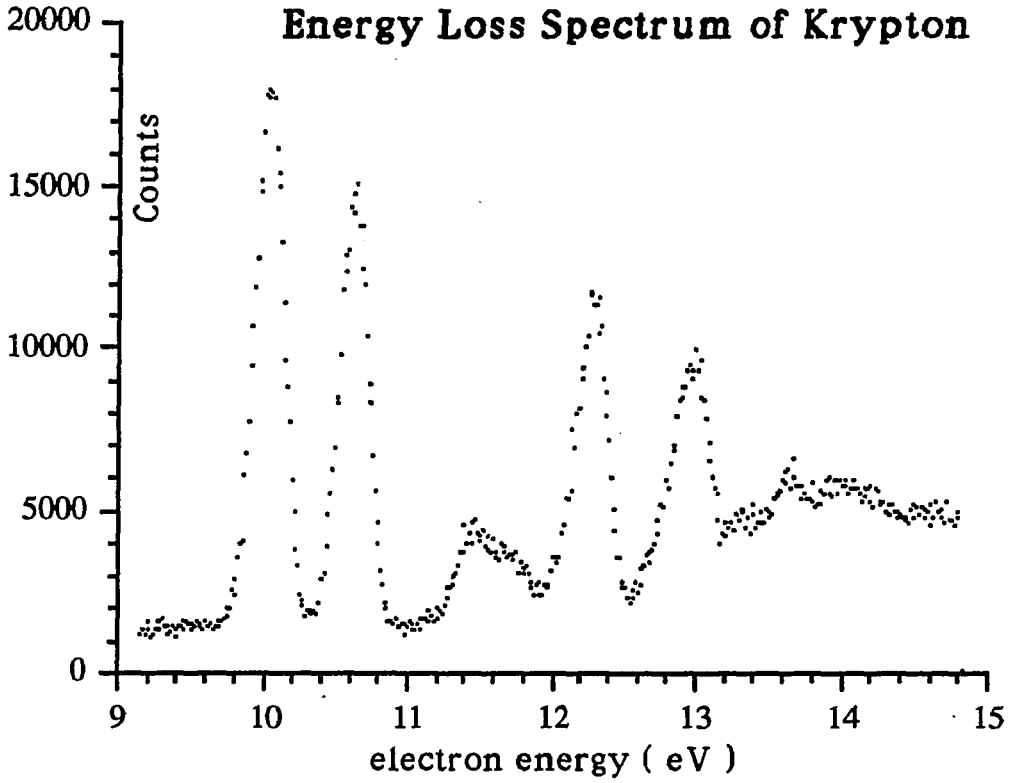

Figure 5.1.2: The energy loss spectrum of krypton at an impact energy of 50 eV and a scattering angle of 7.5°.

about 200 Hz at the largest scattering angles studied in this thesis. Photon count rates range from 100 Hz 800 Hz and include in some cases significant contribution comes from rare gas ion line emissions, since we do not employ any wavelength selection in the photon channel. Both count rates can be varied by changing the beam current and/or the energy resolution of the incident electron beam by varying the aperture size in the electron monochromator (and in the electron analyzer) and by changing the transmission energy. We typically used aperture sizes of 1.0 - 1.7 mm and the transmission energies 12 - 20 eV in the energy selector of both the monochromator and the analyzer. With these settings, the incident electron beam current ranged from 5 to 150 nA.

§5.2 The Alignment of the Electron Beam and the Calibration of the Scattering Angle

The mechanical backlash in the bevel gear arrangement which rotates the electron analyzer in our experimental setup is about ±0.5°. The accuracy of the electron scattering angle is determined mainly by the accuracy with which the forward scattering direction can be determined.

Three independent experimental checks are made to determine the forward direction using

1) the mechanical alignment of the electron spectrometer with a HeNe laser using holes in back of the spectrometer selectors, the monochromator exit aperture, and the analyzer entrance aperture

2) the unscattered straight-through electron current measured on a Farady cup placed behind the exit hole of the energy selector in the analyzer.

3) the measurements of the P_2 coherence parameter at small scattering angles θ_e and $-\theta_e$ about the forward direction

The following description highlights the procedure:

1) A hole of about 1.0 mm was drilled in the back section of the energy selector in the monochromator in line with the electron beam path leaving the monochromator. A HeNe laser (ML810, Metrologic Instruments Inc.) beam is shone through a hole and the cylindrical exit aperture of the monochromator. The laser beam goes through the center of the interaction region and enters the analyzer through an entrance aperture. A hole in the back the analyzer energy selector was enlarged to a slot of about 0.25 cm × 1.0 cm.

The mechanical alignment of the spectrometer is checked by monitoring the diffraction pattern of the laser beam on a screen about 5 m behind the electron spectrometer. The mechanical alignment is considered acceptable when the diffraction pattern consists of only a few symmetric rings. In addition, it is ensured that the electron beam axis is aligned perpendicular to the axis of rotation of the electron analyzer. Both adjustments can be done with an accuracy of ±0.5°.

This alignment procedure is carried out without the electron beam in place and is only considered to be a crude mechanical alignment.

2) Subsequently, a Farady cup is mounted behind the exit hole in the back of the analyzer energy selector. Once the apparatus has been evacuated and the electron beam has been turned on, the Farady cup is used to measure the unscattered straight-through current into the analyzer as the analyzer is rotated through the forward scattering direction. Figure 5.2.1 shows the result of such measurement The position of the maximum current is identified as the forward scattering direction.

Depending on the aperture size and the beam energy and resolution, typical peak current measurements in the Farady cup ranged from 5 to 150 nA, and the fwhm width of the incident electron beam current was 2.5° - 3.5°. This second independent determination of the forward scattering direction can be carried out with a ±0.5° precision. In all cases, it was found that the angular position of the peak current agreed with the mechanically determined forward direction to within ±0.75°.

The alignment using this approach is not carried out under the exact operational conditions in the experiment because voltages applied to the various elements of the electron spectrometer differ from the voltages applied under typical operational conditions. Therefore, the forward direction obtained by this approach cannot be

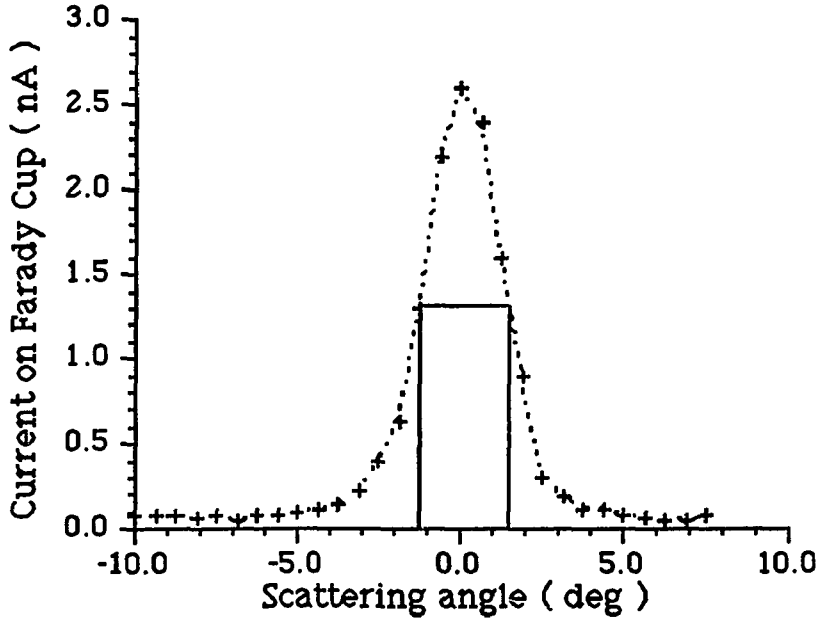

Figure 5.2.1: The measurement of the current on the Farady cup as a function of scattering angle near the forward direction. The fwhm width is about 2.5°.

considered the most reliable one.

3) Symmetry consideration mandate that the linear polarization parameter P_2 is zero in the forward direction (scattering angle $\theta = 0°$), and that:

$$P_2(\theta_e) = - P_2(-\theta_e) \qquad (5\text{-}2\text{-}1)$$

as discussed by Andersen et al. [1988].

In the region of small scattering angles $|\theta_e| \leq 10°$, the P_2 vs θ_e dependence can be approximated by a linear function [Andersen et al. 1988] through the point $P_2 = 0$ at $\theta_e = 0$. Based on the forward direction obtained by the previous two methods, we measured the P_2 parameter at a small positive scattering angle and at a small negative scattering angle with high statistical accuracy. Assuming a linear P_2 vs θ_e dependence, we determined the zero-scattering-angle position with an uncertainty of about $\pm 1°$ from these measurements. It should be noted that the direct search for the zero-scattering-angle by trying to find $P_2 = 0$ is impractical, because the signal count rates at very small scattering angles ($|\theta_e| < 3°$) are very high, so that the channeltron deteriorates in a short time.

We consider the forward direction derived from the small-angle P_2 measurement to be the most accurate and reliable one, since it is carried out under realistic experimental conditions. We note that the angular positions of the forward scattering direction obtained from the other two approaches were found to deviate by no more than $\pm 1.5°$ from the forward scattering direction derived from the small-angle P_2 measurement.

Based on the mutual agreement of the three approaches described above, we believe confident that the forward scattering direction was determined with an

accuracy of ±1.5°. All scattering angles were referenced to the forward scattering direction. Given the unavoidable mechanical backlash in the rotary motion feedthrough, the accuracy and reproducibility for the non-zero electron scattering angles is put at ±2.5°.

§5.3 Operation of the VUV Reflection Polarization Analyzer

The VUV polarization analyzer [Zetner et al. 1983, 1984, Westerveld et al. 1985] is mounted above the interaction region along an axis perpendicular to the scattering plane. The distance between the interaction region and the surface of the first gold mirror is about 3.5 cm. All linear polarization measurements were carried out with a single-reflection device consisting of one optically flat gold-coated mirror mounted at an angle of incidence of 60° in front of a CEM. The advantages of using gold as a reflector material for the VUV reflection polarization analyzer are:

1) gold is a very stable material in vacuum

2) gold has a relatively high overall reflectivity (about 30% at a 60° angle of incidence)

3) the polarization sensitivity (for a single reflection) is relatively high (almost 60% at 75 nm) and it does not change rapidly in the wavelength region 50 -130 nm [Zetner et al. 1983, 1984, Samson 1967].

The alignment and calibration of the VUV polarization detector is initially carried out by measuring the non-coincident radiation pattern of the He 58.43 nm resonance radiation at a fixed impact energy (typically 50 eV) as a function of the angle of the polarizer orientation. Figure 5.3.1 shows the He radiation pattern at 50 eV. The VUV radiation produced by electron impact on He consists essentially of the $n^1P_1 \rightarrow 1^1S_0$ photons with the 58.43 nm photons corresponding to the n = 2 transition dominating. The theoretical prediction for the radiation pattern was presented in Chapter 3. The radiation pattern clearly identifies the directions parallel and perpendicular to the electron beam direction with the accuracy of better than ±5°.

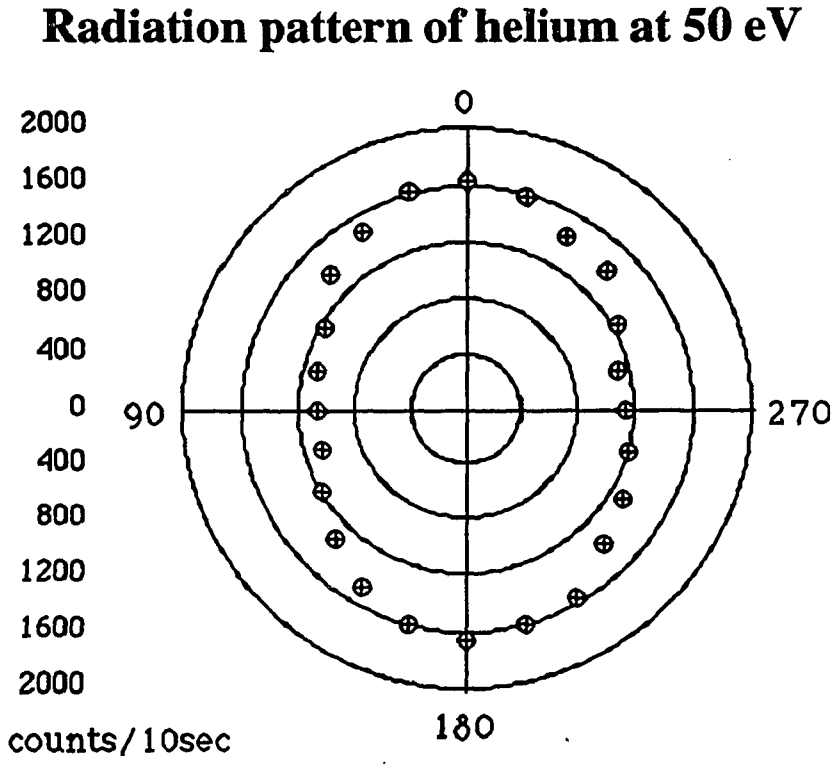

Figure 5.3.1: The radiation pattern of helium at electron impact energy of 50 eV is shown here. The backing pressure of Helium is 0.02 Torr. The view of this diagram is from top of the electron scattering plane. The angular positions correspond to those used in equation (5-4-2) on page 68.

The polarization efficiency of our single-reflection polarization analyzer is determined from:

$$\beta P = \frac{major\ axis - minor\ axis}{major\ axis + minor\ axis} = \frac{I(0°) - I(90°)}{I(0°) + I(90°)} \qquad (5\text{-}3\text{-}1)$$

where β is the polarization sensitivity of the reflection polarizer. P is the actual linear polarization of the emitted He radiation. The linear polarization of the He resonance radiation has been measured [Hammond et al. 1989] and calculated [Csanak and Cartwright 1989]. At 50 eV, the measured and calculated values of the linear polarization agree to better than 3%. Furthermore, contributions to the photon signal from higher n^1P_1 He states do not influence the polarization. Experimental studies [Hammond et al. 1989] and theoretical calculations [Csanak and Cartwright 1989] reveal virtually no n-dependence for the polarization. For the case displayed in figure 5.3.1, $\beta P = 0.296$ and $P = 0.52$ [Csanak and Cartwright 1989] lead to a polarization sensitivity $\beta = 0.57 \pm 0.02$.

Subsequently, we used a different (and easier to implement) approach to determine the polarization sensitivity of our polarization analyzer. Once we had established experimentally that the P_1 coherence parameter in the forward scattering direction always yielded a value of $P_1 = +1$, we based further determinations of the polarization sensitivity on P_1 measurements in the forward scattering direction. Typical values of the polarization sensitivity ranged from 0.59±0.02 at 75 nm to 0.68±0.02 at 125 nm depending on the surface clearliness in addition to the wavelength.

§5.4 Data Acquisition

Two identical lines of fast pulse counting electronics shape the output pulses from the electron and photon channeltrons separately to enable the acquisition of coincidence spectra with nanosecond time resolution. The output pulses from the electron and photon channels resulting from identical scattering events arrive with a fixed time delay which produces a narrow peak in the time spectrum. Uncorrelated events result in chance coincidences which produce a flat background in the time spectrum.

Figure 5.4.1 is a schematic diagram of the coincidence electronics. The signals are processed by two identical circuits amplifying and shaping the CEM pulses. One signal eventually triggers the "start" of a time to amplitude converter (TAC) and the second channel after a suitable delay triggers the "stop". The output of the TAC converter is stored in a multichannel analyzer operated in the pulse height analysis mode and subsequently transferred to a Macintosh II computer for permanent storage and for further data analysis.

The output from the channeltron CEM is a current pulse floating on top of the CEM high voltage. The circuit in figure 5.4.2 decouples the signal from the high voltage utilizing a simple capacitor. The voltage output from the decoupling box is approximately 20 mV and is amplified by a charge sensitive fast preamplifier with a voltage gain of approximately 10. The signal is further amplified and shaped by a delay line amplifier with a gain ranging from 3 to 1000. The delay line amplifier subtracts from the signal a suitably delayed replica of the input signal resulting in a pulse with a 1 msec width.

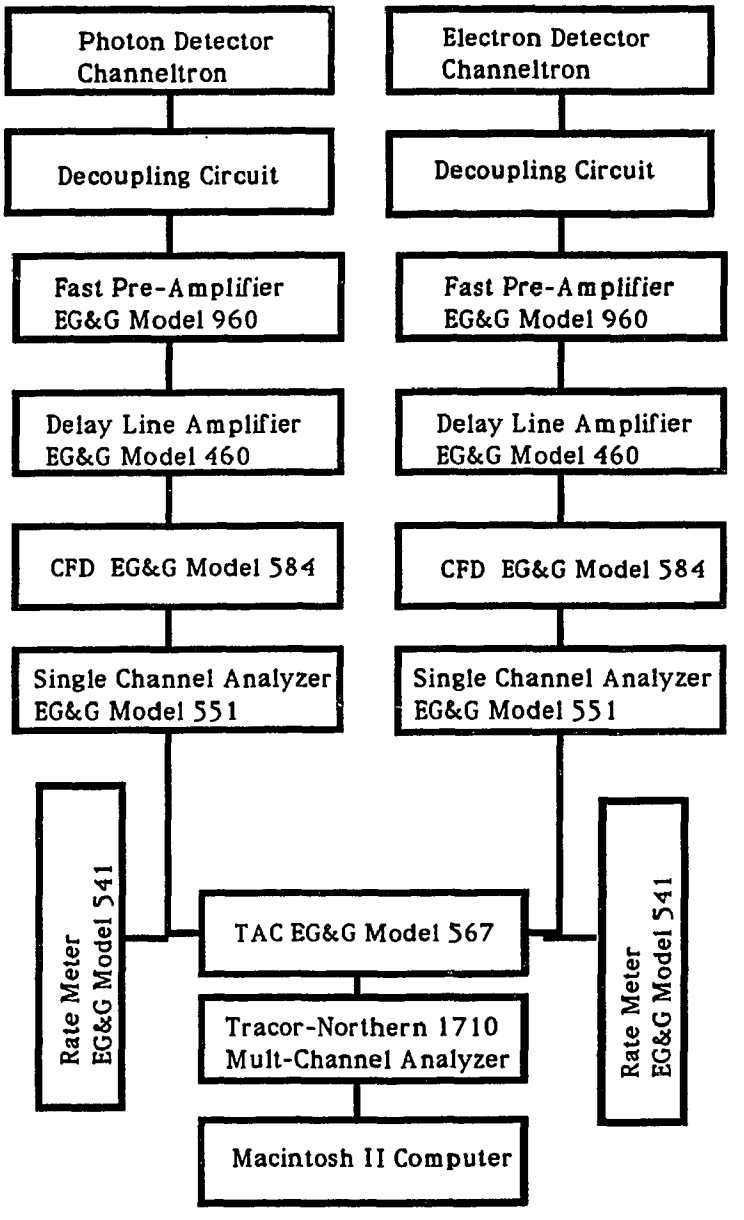

Figure 5.4.1: Schematic diagram of the coincidence electronics.

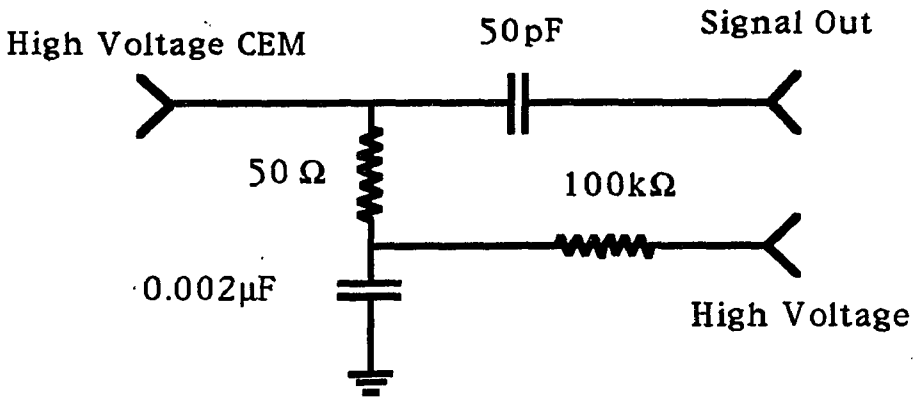

Figure 5.4.2: The signal decoupling circuit. The signal at the back of the channeltron is decoupled from the CEM HV by the 50pF capacitor.

A very important feature of the signal processing circuit is the timing. Most signals have different amplitudes and leading edges. The constant fraction discriminator (CFD) eliminates signals below a threshold and triggers an output at a given fraction of the input signal. The constant fraction technique subtracts from the delayed input signal a fraction of the input signal. The zero crossing of the result, which occurs at the same fraction of the input maximum regardless of its amplitude, triggers a fast output pulse.

A timing single channel analyzer (SCA) introduces a variable delay in the two channels ranging from 100 ns to 11 μsec. The time delay between the pulses is converted to a voltage in the time-to-amplitude converter (TAC). A start pulse from one channel triggers a ramp voltage and a suitably delayed pulse from the second channel triggers the stop. The stop pulse clamps the ramp voltage and relays the amplitude to the output of the TAC. If no stop pulse arrives within a designated time interval (500 ns), the ramp resets and awaits another starting pulse or trigger. A multichannel analyzer (MCA) in the pulse height analysis mode accumulates the data. The inherent time resolution of the coincidence electronics, which is obtained when both channels are supplied with the same standard pulse from a pulse generator, is below 1ns. The operational time resolution of the apparatus was found to be 6 -15 ns which largely results from the jitter in the transition time of the pulses detected and amplified by the channeltron detectors and from the time spread of the scattered electrons as they travel through the energy analyzer.

The MCA, in addition to acquiring data, controls the polarization angle of the photon detector. Data are collected for 200s (or 500s) in one polarizer position. The MCA then triggers a stepper motor which rotates the analyzer by 90° to collect data

in the other polarizer position. The data for each polarization position are stored in separate memory locations in the MCA. The MCA triggers the stepper motor controller a second time to return the polarizer to the first angle after another 200s (or 500s). The cycle is repeated until accumulation in each channel reaches a fixed preset data accumulation time. This process ensures that long term drifts in the electron beam current and gas beam density do not produce a systematic error in the determination of the polarization correlation parameter.

Figure 5.4.3 shows an Ar "$^1P_1$" coincident spectrum at a scattering angle 10° and an incident electron impact energy 40 eV.

The determination of the true coincidences for the spectrum displayed in figure 5.4.3 is rather straightforward. The area of the peak above a constant background due to the chance coincidences represents the number of true coincidences $I(\theta)$, where θ denotes the orientation of the polarizer axis relative to the electron beam axis. The background is determined on either side of the coincidence peak. If the two background determinations on the two sides of the coincidence peak differed by more than one standard deviation, we assume that systematic drifts had affected the measurement and disregarded the data. In the same way, the true coincidences for the second polarizer orientation is denoted by $I(\theta+90°)$.

The apparent linear polarization is

$$P_{app} = \frac{I(\theta) - I(\theta+90°)}{I(\theta) + I(\theta+90°)} \qquad (5\text{-}4\text{-}1)$$

where $\theta = 0°$ denotes the measurement of the linear polarization P_1 and $\theta = 45°$ denotes the measurement of the linear polarization P_2. The true linear polarization parameters P_1 and P_2 are

Figure 5.4.3

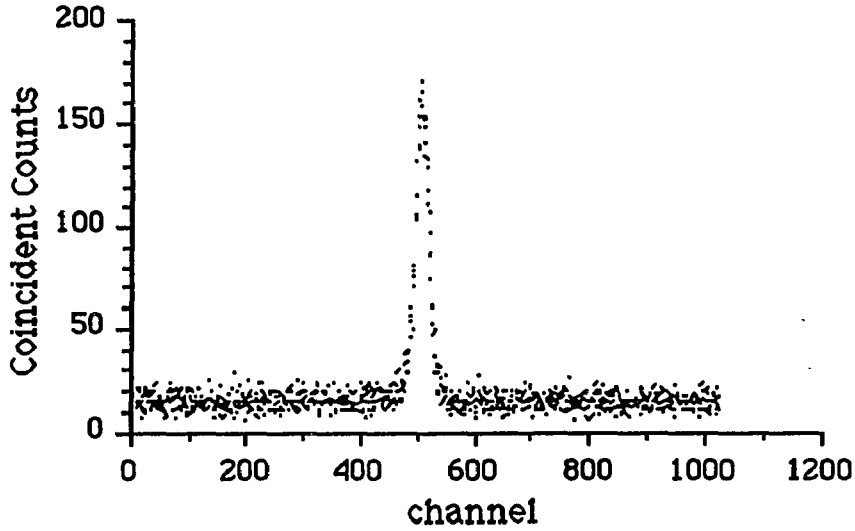

This is coinsident spectrum of one channel for "$^1P_1$"excitation in Ar at 50 eV and at 10 °.

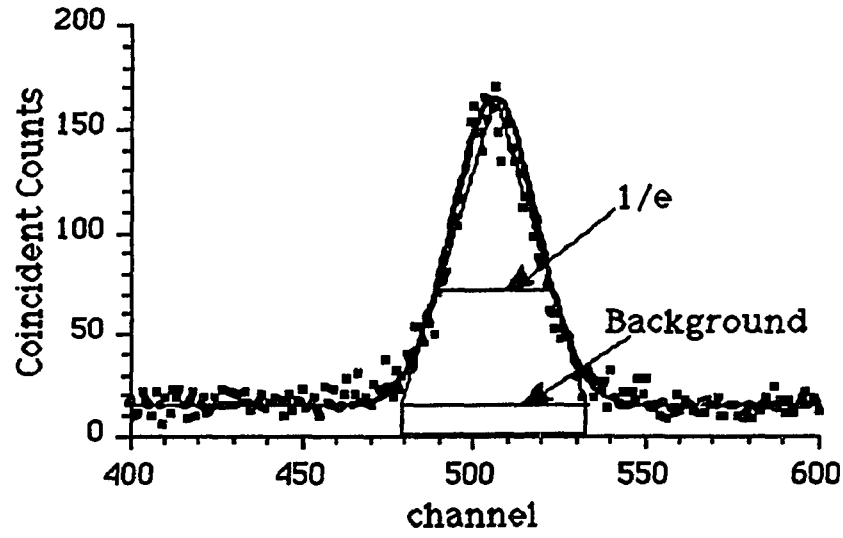

Also shown is a Gaussian fit to the peak and the background area for the error determination. See text for details.

$$P_{1,2} = \frac{1}{\beta} \frac{I(\theta) - I(\theta+90°)}{I(\theta) - I(\theta+90°)} \qquad (5\text{-}4\text{-}2)$$

The lifetimes of the excited "$^1P_1$" and "$^3P_1$" states for the heavy noble gases which we investigated [see table 3.1.1] are less than the operational time resolution of the apparatus, which is about 6 - 15 ns as stated before. The collisional excitation process (10^{-15} sec) can be considered instantaneous. Therefore, we do not expect to see the exponential decay due to the lifetime of the excited state in the coincidence spectrum.

The statistical uncertainty of a linear polarization measurement is calculated according to standard propagation techniques (Bevington 1969):

$$\sigma^2 = \frac{1}{\beta^2} \frac{4}{(I_1 + I_2)^4} [I_2^2(I_1+2B_1) + I_1^2(I_2+2B_2) + \frac{\delta_\beta^2}{4\beta^2}(I_1^2+I_2^2)^2] \qquad (5\text{-}4\text{-}3)$$

where,

β = polarization sensitivity

δ_β = uncertainty in the polarization sensitivity

I_1 = number of true coincidences $I(\theta)$

I_2 = number of true coincidences $I(\theta+90°)$

B_1 = background at θ

B_2 = background at $\theta+90°$

Equation 5-4-3 is derived assuming Poission counting statistics. The first two terms in the equation are due to the uncertainty in the determination of the two peak areas while the last term reflects the uncertainty in the determination of the VUV polarization efficiency. Typically, the last term contributes less than ten percent to the overall uncertainty.

Further discussion regarding the determination of quantities B_1 and B_2 is warranted, since the size of the region of interest which is used to determine the peak area is arbitrary. While the size of the region of interest will not affect the value of P_{app} (as long as the region is wide enough to encompass the entire peak), its size will affect the determination of B_1 and B_2. If the region is too wide and extends beyond the base width of the true coincidence peak on either or both sides, then obviously B_1 and B_2 will be too large. This does not affect the value of P_{app}, but it would overestimate the uncertainty according to equation (5-4-3). Therefore, the reliable determination of σ^2 relies on the ability to determine the base width of the coincidence peak reliably and reproducibly.

The actual coincidence peak is a convolution of the time resolution of the detectors and the electronics which is very close to a Gaussian and a decaying exponential part which is due to the lifetime of the excited state. Even though the lifetime is typically considerably smaller than the apparatus function, its presence leads to a slightly asymmetric coincidence peak with an enhanced maximum compared to a Gaussian in most cases as shown in figure 5.4.3.

The practical fitting of a suitable mathematical function to the coincidence spectrum is non-trivial and contributes no additional physical insight. We have to stress that the quality of our Gaussian fit does not at all influence the determination of P_{app} and its influence on the determination of B_1 and B_2 and hence of σ^2 is marginal. We used a Gaussian fit to the coincidence spectra in an attempt to determine the base width of the peak for the calculation of B_1 and B_2. Once the 1/e-width was established, the base width of the coincidence peak is determined from the intersection of the extrapolated triangle defined by the peak height of the fit and the 1/e-width with

the background level in the coincidence spectrum shown in figure 5.4.3.

We note that coincidence spectra obtained at larger scattering angles and lower impact energies did not exhibit the same good signal-to-background ratio as the one displayed in figure 5.4.3. In those cases, the Gaussian fit provided a poor fit to the actual spectrum, but it still served as a reliable means of determining the background counts.

Chapter 6 The Instrumental Effects

Before the experimental data are presented and discussed, we will discuss the effects of instrumental and other physical effects on the measured data, so that a meaningful comparison with theoretical predictions can be made. This discussion includes the effects of a depolarization of the emitted radiation due to hyperfine structure, the influence of the finite acceptance of the electron analyzer and the photon detector and the influence of the finite volume of the interaction region.

We note that all polarization correlation parameters measured as part of this thesis were obtained at pressures where radiation trapping effects were negligible and under conditions where the photon count rate varied linearly with the gas pressure and the electron beam current. A detailed investigation carried out as part of a previous thesis [Martus 1990] established the experimental conditions for a reliable determination of linear polarization correlation parameters in all three gases Ne, Ar and Kr. All measurements carried out as part of this thesis were carried out within the previously established experimental conditions.

§6.1 The Depolarization due to the Hyperfine Structure

While natural Ne and Ar consist only of isotopes with zero nuclear spin, natural Kr consists to 11.5% of an isotope Kr^{83} with nuclear spin I = 9/2. As stated in chapter 3, the lifetime of the excited states is sufficiently long for the hyperfine angular momentum recoupling to occur which leads to a depolarization of the emitted radiation. The effects of the depolarization due to hyperfine structure is not included in the published theoretical predictions for Kr [Bartschat and Madison 1987, Meneses et al. 1985, 1991]. Therefore, the polarization correlation parameters P_1, P_2, P_3 and P_4, which relate to the nascent excited state intermediately after the excitation have to be modified to include the effects of hyperfine depolarization [Nienhuis 1980]:

$$P'_1 = \frac{3G_2(1-\rho_{00})}{2 + G_2(1-3\rho_{00})} P_1$$

$$P'_2 = \frac{3G_2(1-\rho_{00})}{2 + G_2(1-3\rho_{00})} P_2$$

$$P'_3 = \frac{3G_1(1-\rho_{00})}{2 + G_2(1-3\rho_{00})} P_3$$

$$P'_4 = \frac{G_2(1-3\rho_{00}) + G_2(1-\rho_{00})P_1}{\frac{4}{3} - \frac{1}{3}G_2(1-\rho_{00}) + G_2(1-\rho_{00})P_1}$$

where P'_1, P'_2, P'_3, and P'_4 are the time-averaged measured polarization correlation parameters. G_1 and G_2 are the appropriate depolarization factors for the P-S transition in question [Blum 1981, Andersen et al. 1988] and can be found, for example, in the paper of Corr et al. [1991]. Table 6.1.1 lists the G-factors and their effects on the coherence parameters.

Tabble 6.1.1: The depolarization factors G_1, G_2 for the P-S transition. See the text for details.

	G_1	G_2	Abundance in nature
Kr^{83}	0.347	0.208	11.5%

The depolarization due to the hyperfine structure will be taken into account in the theoretical predictions for Kr in the later discussion.

§6.2 The Depolarization due to Instrumental Effects

The intersection of the electron beam and the gas beam produces an extended interaction volume of a few mm^3. The effects of a finite interaction volume on the measured coherence parameters have been investigated recently in series of papers [Simon et al. 1990, Zetner et al. 1989, 1990, Corr et al. 1991, van der Burgt 1991]. The different groups reached similar conclusions.

The finite interaction volume can influence the measured parameters in a variety of ways through:

1) a small dispacement of the electron beam relative to the electron analyzer vertically or horizontally caused by a mechanical misalignment or by the electrostatic deflection of the electron beam.

2) a non-uniform electron distribution (electron density profile) within the electron beam due to beam focusing effects

3) a non-uniform gas density profile on the interaction region due to the use of a gas jet from a capillary source or a small misalignment

4) finite acceptance angles of both the electron analyzer and the photon polarization analyzer.

The finite acceptance angles of the electron analyzer and the photon detector present a problem that would be relevant even for a point-like interaction region. The influence of the finite angular acceptance of the electron analyzer has been discussed in detail by Martus, Becker and Madison [1989, 1990] and was found to be significant only in the forward scattering direction or in scattering regions where the measured parameters pass through a maximum or minimum very rapidly as a function of

the electron scattering angle. The influence of the finite angular acceptance of the VUV polarization analyzer (photon detector) has been analyzed by Corr et al. [1991] who demonstrated that no significant effects occur for the small acceptance angles that are typically used with this kind of detector.

In order to deal with the remaining finite volume effects it would be desirable to establish a procedure that allows us to correct a set of measured coherence parameters for all residual instrumental effects. It has not been possible to achieve this goal to date. What has been accomplished is a numerical procedure that predicts how a given set of nominal parameters would be influenced by the presence of instrumental effects. We will briefly present the basic idea of this approach which was developed by van der Burgt et al. [1991]. The model of van der Burgt et al. represents the finite volume of the intersection of the electron beam and the gas beam by a three-dimensional equidistant array of discrete points (cubic lattice) where the distance between adjacent array points can be chosen arbitrarily. The intensity of the light reaching the detector perpendicular to the nominal scattering plane (for the measurements of P_1, P_2 and P_3), and another detector in the nominal scattering plane and perpendicular to the incident electron beam (for the measurement of P_4) is calculated for each array point. Each array point corresponds to a different polarization radiation pattern of the photons and differential cross section due to a slight deviation of the electron scattering angle. The density of gas jet at that array point is implemented by assigning a weight factor. The finite acceptance angles of the electron analyzer and photon polarization analyzer are also implemented in the model. The total intensity is obtained by summing over all array points.

It was found that the polarization correlation parameters P_1, P_2 and P_3 measured perpendicular to the scattering plane were affected only in a very minor way, but that serious perturbations of the polarization parameter P_4 could occur. It was also found that the measured P_4 parameter was most susceptible to finite interaction volume effects at small electron scattering angles and/or at scattering angles where the P_1 parameter is close to a value of -1. We note that other approaches, e.g. Simon et al. [1990], are equally valid and lead to similar results and conclusions. A detailed discussion can be found in the recent review paper by Becker et al. [1992]. Lastly, a somewhat crude and simplistic approach to the more complex "inverted" problem of correcting a set of measured parameters for the instrumental effects was proposed by van der Burgt et al. [1991] who developed approximate analytical expression between the measured Stokes´ parameters and the corrected time-averaged nominal Stokes´ parameters. Since this approach is apparatus specific, we will not discuss it further here.

Up to now, our experiment has been measuring primarily the polarization parameters P_1 and P_2 (and recently P_3) perpendicular to the scattering plane. In the light of the above discussion of instrumental effects due to the finite volume of the interaction region, we estimate that the corrections caused by these effects in our apparatus are much smaller than the statistical uncertainty in measured data.

Chapter 7 Experimental Results and Discussion

The experimental data will be presented and discussed in the following order:

1) "$^1P_1$" excitation in Ne, Ar, and "$^3P_1$" excitation in Kr at an electron impact energy of 50 eV and electron scattering angles up 40°.

2) "$^1P_1$" excitation in Ar at electron impact energies of 50 eV, 40 eV, 30 eV and 25 eV and scattering angles up to 55°.

3) "$^3P_1$" excitation of Kr at an electron impact energy of 30 eV and scattering angles up to 55°.

The motivation for these particular measurements was

1) a comparative study of the excitation of a state that is predominantly of singlet character in the regime of large impact parameter for Ne, Ar and Kr

2) a systematic study of how the level of agreement between experiment and theory changes as one goes to smaller electron impact energies where the first-oder perturbative theories are no longer expected to provide an adequate description of the excitation process

3) a test whether the level of agreement between experiment and theory at the lower impact energy is target dependent

§7.1 Excitation of the ns'[1/2]$^0_1$ State in Ne (n=3) and Ar (n=4) and of the 5s[3/2]$^0_1$ State in Kr at 50 eV

It can be seen from the singlet-triplet mixing coefficients (see table 3.1.1) that the three states under investigation are predominantly of singlet character.

Figure 7.1.1 shows the measured P_1 and P_2 parameters for "$^1P_1$" excitation in Ne at 50 eV and scattering angles up to 40°. Predictions from both first-oder perturbative theories, the DWBA and the FOMBT, are shown together with the FBA and compared to the measured data. The RDW prediction has been omitted from the figures, since it is very similar to the DWBA (This was found to be true for all situations studied in the course of this thesis and, therefore , the results of the RDW calculations have been omitted throughout). All data have been corrected for instrumental and other effects to the maximum extent possible. The error bars shown include all known systematic uncertainties and one standard deviation of counting statistics. No horizontal error bars have been indicated for clarity of presentation. We note that the uncertainty in the electron scattering angle is ±2.5°.

The experimental P_1 data show a decline from $P_1 = 1$ in the forward direction to minimum of around -0.8 at a scattering angle of about 25°, followed by a steady rise towards large value of θ_e. The FBA, a comparatively simplistic theory, provides an adequate description of the experimental P_1 data up to $\theta_e = 25°$. There is good agreement between the measured P_1 data and the theoretically predicted values of both the DWBA and the FOMBT at scattering angle below 25°. For scattering angles above 30°, the measured P_1 parameter increase as predicted by the DWBA and the FOMBT, but the agreement is rather poor. Our P_1 measurements show a slightly better agreement with the DWBA at scattering angles above 30°.

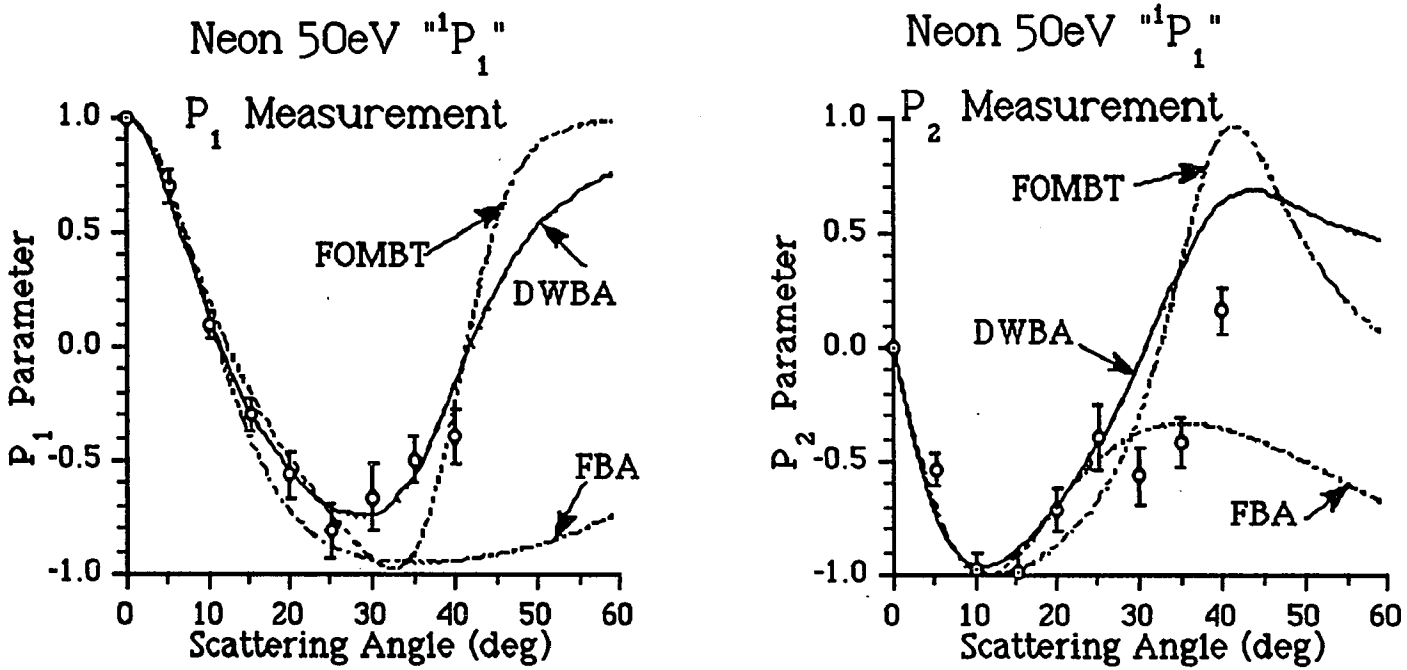

Figure 7.1.1: P_1 and P_2 polarization correlation parameters for excitation of the $3s'[1/2]_{J=1}$ state in Ne at 50 eV as a function of electron scattering angle. Error bars include all known systematic uncertainties and one standard deviation of counting statistics. For clarity, no horizontal error bars are indicated.

The measured P_2 parameters decline from $P_2 = 0$ in the forward scattering direction to a minimum of $P_2 \approx -1$ at a scattering angle of 10°, and then increase monotonically except for the data around 30°. There is good agreement between the measured and the calculated P_2 values from both the DWBA and the FOMBT as well as with the FBA up to a scattering angle of 25°. Above 25°, however, the measured P_2 parameters diverge quite dramatically from both the DWBA and the FOMBT predictions. Given the inherent short-coming of the FBA, the apparent agreement of the P_2 data at 30° and 35° can only be viewed as coincidental. We note that the simplistic FBA cannot be expected to provide an adequate description of the scattering process. We found that the FBA failed to reproduce the general features of the measured data for all but the smallest scattering angles. It is interesting to note in that context that the range of validity of the FBA decreases with increasing complexity of the target atom from He to Ne to Ar to Kr [Andersen et al. 1988, and discussion later].

Figure 7.1.2 shows the two natural parameters, the alignment angle γ and the linear polarization P_{lin}^{+}, extracted from P_1 and P_2 as a function of the electron scattering angle. Up to a scattering angle of 25°, the experimentally determined alignment angles follow the theoretical prediction of all three theories (which are virtually indistinguishable in that scattering region) quite closely. The deviation of the measured alignment angle γ and the theoretical predictions at scattering angles above 30° is, however, considerably less dramatic than one might expect on the basis of the significant discrepancy between the measured and calculated P_1 and P_2 parameters. This might indicate that the alignment angle is a parameter which is rather insensitive to the details of the collision precess.

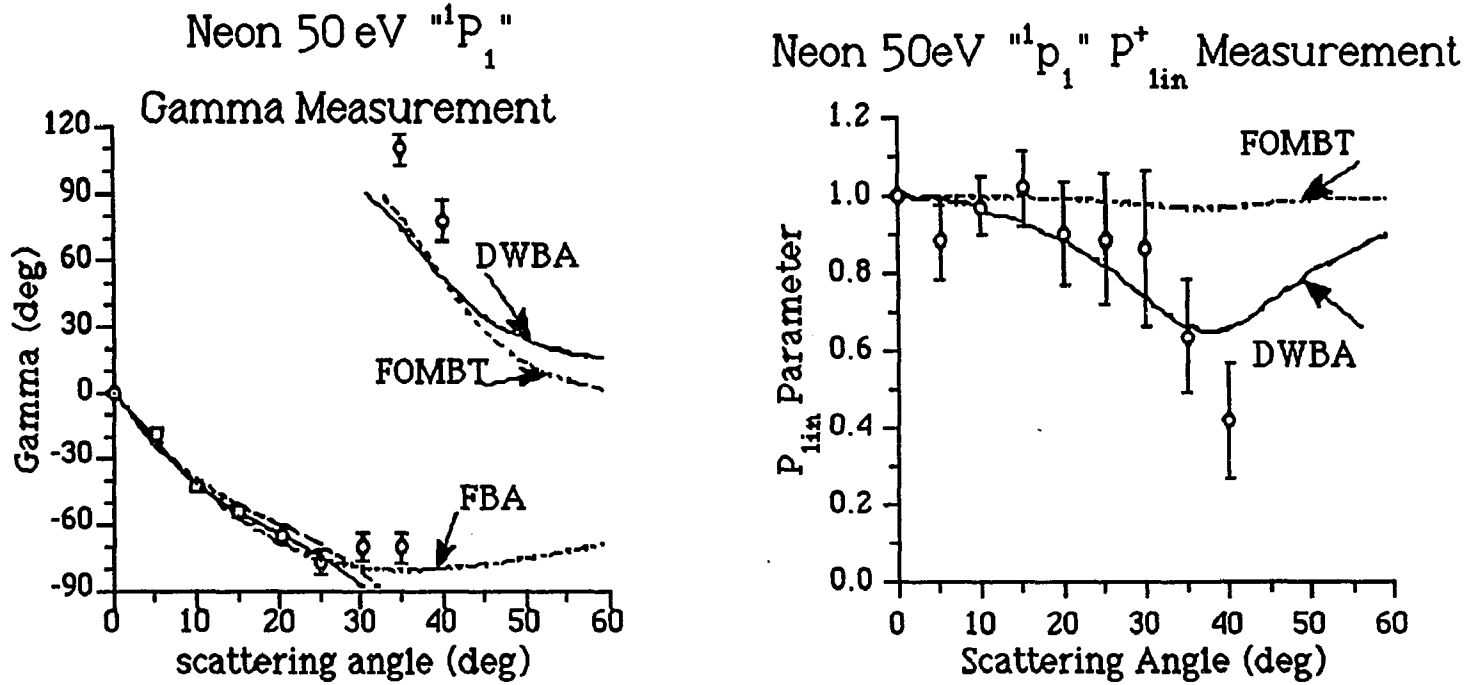

Figure 7.1.2: Alignment angle γ and linear polarization P^+_{lin} for excitation of the $3s'[1/2]_{J=1}$ state in Ne at 50 eV as a function of electron scattering angle. Error bars include all known systematic uncertainties and one standard deviation of counting statistics. Where no error bar is indicated, the uncertainty is smaller than the plot symbol. For clarity, no horizontal error bars are indicated.

We note that two γ values have been displayed at a scattering angle of 35° for clarity of presentation. In addition to the value γ = -70°, we include a second value of γ = 110° (even though it lies outside the commonly used -90° to 90° range of γ values) shifted by 180° which was included to highlight the trend in the experimentally determined values of the alignment angles γ as a function of electron scattering angle.

In contrast to the case of the alignment angle γ, the DWBA and the FOMBT predictions for the P_{lin}^{+} parameter are distinctly different. The DWBA predicts a significant drop from P_{lin}^{+} = 1 at scattering angles below 15° to a value of about 0.65 at a scattering angle of about 40°, whereas the FOMBT suggest P_{lin}^{+} values much closer to 1 over the entire range of the scattering angle up to 60°. Our experimental values for P_{lin}^{+} in Ne at 50 eV are consistent with a drop at scattering angles above 20° and thus support the prediction of the DWBA.

The experimentally determined parameters for "$^1P_1$" excitation in Ne at 50 eV are also summarized in Table 7.1.1.

Figure 7.1.3 shows the measurements of the P_1 and P_2 parameters for the excitation of $4s'[1/2]^0_1$ state in Ar at 50 eV and scattering angles up to 40°. The theoretical predictions of all three approaches (FBA, DWBA and FOMBT) also appear in figure 7.1.3.

The experimental values of the P_1 parameter decline to the minimum of -0.68 at a scattering angle of 20° from P_1 = 1 in the forward direction, and then gradually increase. The values of P_2 also decline to a minimum of $P_2 \approx -1$ at a scattering angle between 5° and 10°, and then rapidly increase to the maximum of 0.67 at a scattering angle of 25° followed by a slow decline towards large values of θ_e. Considering the

Table 7.1.1: Coherence parameters P_1 and P_2 for excitation of the $3s'[1/2]_{J=1}$ state in Ne at an impact energy of 50 eV and various electron scattering angles. Given are the nominal values of P_1 and P_2 corrected for all instrumental effects, where necessary, along with the extracted values for the alignment angle γ and the linear polarization P^+_{lin}. The quoted errors include all systematic uncertainties and one standard deviation of counting statistics.

Scattering angle (deg)	P_1 Parameter	P_2 Parameter	Alignment angle γ (deg)	linear Polarization P^+_{lin}
5.0±2.5	0.71±0.07	-0.53±0.07	-8.4±3.1	0.89±0.10
10.0±2.5	0.10±0.06	-0.97±0.07	-42.1±2.0	0.98±0.08
15.0±2.5	-0.29±0.07	-0.98±0.08	-53.2±2.5	1.02±0.10
20.0±2.5	-0.56±0.10	-0.71±0.09	-64.1±4.3	0.90±0.13
25.0±2.5	-0.80±0.12	-0.39±0.14	-77.0±5.7	0.89±0.17
30.0±2.5	-0.66±0.15	-0.56±0.13	-69.8±6.5	0.87±0.20
35.0±2.5	-0.49±0.10	-0.41±0.11	-70.0±6.7	0.64±0.15
40.0±2.5	-0.39±0.12	0.17±0.10	78.2±9.4	0.43±0.15

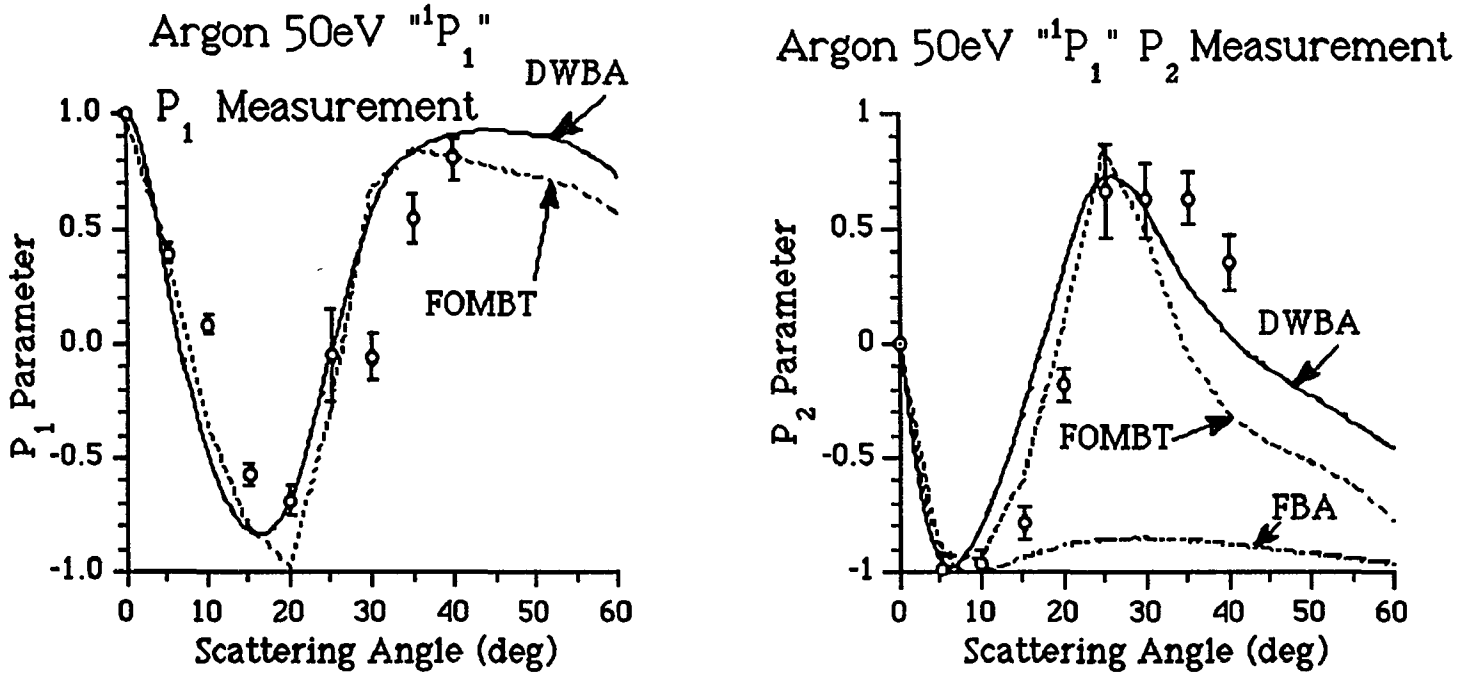

Figure 7.1.3: P_1 and P_2 polarization correlation parameters for excitation of the $4s'[1/2]_{J=1}$ state in Ar at 50 eV as a function of electron scattering angle. Error bars include all known systematic uncertainties and one standard deviation of counting statistics. For clarity, no horizontal error bars are indicated.

uncertainty in the electron scattering angle of ±2.5°, the theoretical predictions for the P_1 and P_2 parameters from both the DWBA and the FOMBT are in quite good agreement with the experimental data at scattering angles up to 25°. For scattering angles above 30°, the general agreement of the measured P_1 and P_2 values with the theories is less satisfactory. The deviation of the P_2 parameter from the theories is less prominent than that of the P_1 parameter.

Figure 7.1.4 shows the alignment angle γ and the linear polarization P_{lin}^+ as a function of electron scattering angle up to 40° for the excitation of "$^1P_1$" state in Ar at 50 eV. The FBA is valid up to scattering angles of 10° for both the P_1 and the P_2 parameter. Up to a scattering angle of 25°, the experimental data of the alignment angle γ are in good agreement with the theoretical predictions. Similar to the case of Ne, the deviation of the experimentally determined alignment angle γ with theoretical predictions is less than that of the P_1 and P_2 parameters which further supports the notion that the alignment angle γ is less sensitive to the details of the collision process. In the electron scattering angle range of 15° - 35°, the experimentally determined linear polarization parameter P_{lin}^+ shows a drop from $P_{lin}^+ = 1$, which is described by the DWBA, so that the measurement of the P_{lin}^+ parameters up to 40° again favors the DWBA.

The experimentally determined parameters are summarized in Table 7.1.2.

Figure 7.1.5 shows the measured P_1 and P_2 parameters for the excitation of $5s[3/2]^0_1$ ("$^3P_1$") state in Kr at 50 eV for scattering angles up to 40°. The theoretical predictions of all three approaches are also shown in the figure.

The FBA describes the P_1 and P_2 parameters of scattering angle up to less than 10°. The DWBA and the FOMBT predictions shows good agreement with the

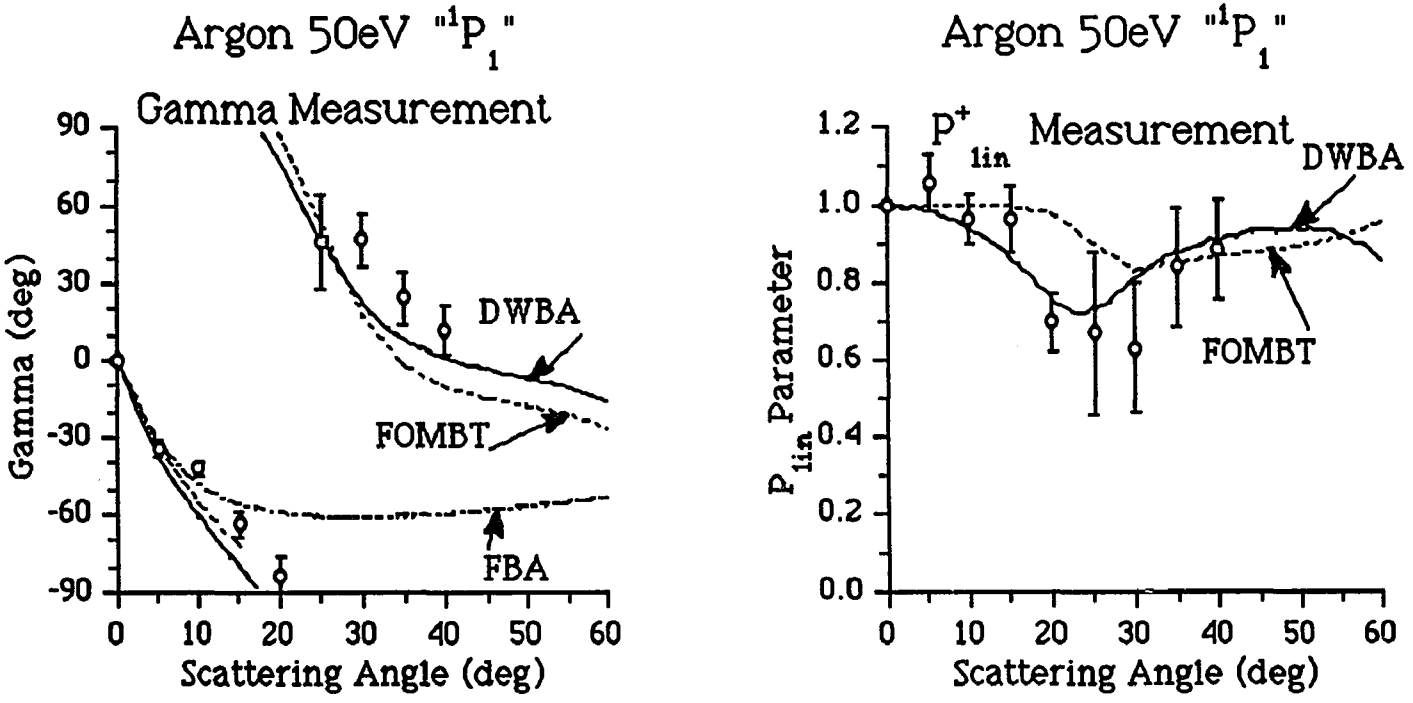

Figure 7.1.4: Alignment angle γ and linear polarization P^+_{lin} for excitation of the $4s'[1/2]_{J=1}$ state in Ar at 50 eV as a function of electron scattering angle. Error bars include all known systematic uncertainties and one standard deviation of counting statistics. Where no error bar is indicated, the uncertainty is smaller than the plot symbol. For clarity, no horizontal error bars are indicated.

Table 7.1.2: Coherence parameters P_1 and P_2 for excitation of the $4s'[1/2]_{J=1}$ state in Ar at an impact energy of 50 eV and various electron scattering angles. Given are the nominal values of P_1 and P_2 corrected for all instrumental effects, where necessary, along with the extracted values for the alignment angle γ and the linear polarization P^+_{lin}. The quoted errors include all systematic uncertainties and one standard deviation of counting statistics.

Scattering angle (deg)	P_1 Parameter	P_2 Parameter	Alignment angle γ (deg)	linear Polarization P^+_{lin}
5.0±2.5	0.40±0.04	-0.98±0.06	-33.9±3.2	1.06±0.06
10.0±2.5	0.11±0.04	-0.96±0.06	-41.7±2.7	0.97±0.06
15.0±2.5	-0.57±0.05	-0.78±0.07	-63.1±4.8	0.97±0.09
20.0±2.5	-0.68±0.06	-0.17±0.07	-83.0±6.7	0.70±0.08
25.0±2.5	-0.04±0.20	0.67±0.20	46.7±18.1	0.67±0.21
30.0±2.5	-0.05±0.10	0.63±0.16	47.3±10.2	0.63±0.17
35.0±2.5	0.55±0.11	0.64±0.11	24.7±10.5	0.84±0.16
40.0±2.5	0.81±0.09	0.36±0.12	12.0±9.4	0.89±0.13

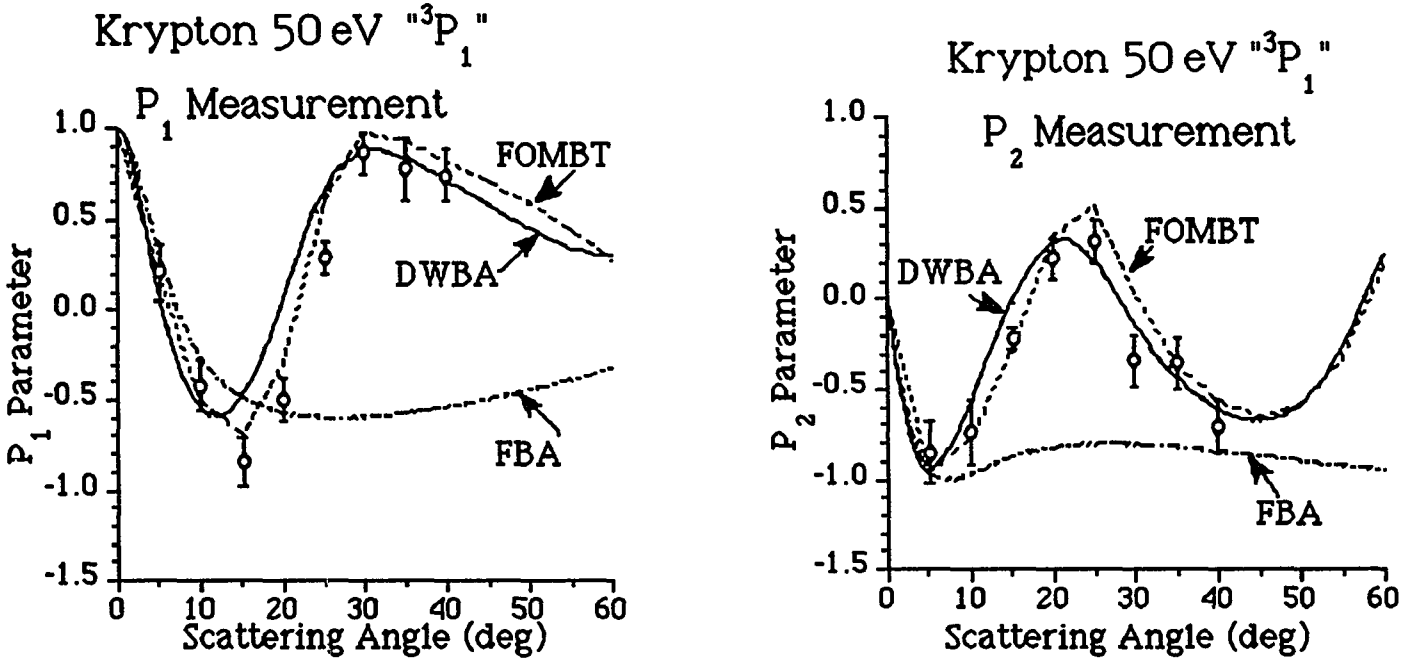

Figure 7.1.5: P_1 and P_2 polarization correlation parameters for excitation of the $5s[3/2]_{J=1}$ state in Kr at 50 eV as a function of electron scattering angle. Error bars include all known systematic uncertainties and one standard deviation of counting statistics. For clarity, no horizontal error bars are indicated.

measured P_1 and P_2 parameters over entire electron scattering angle range studied. A closer look at the measured and calculated P_1 and P_2 parameters suggests that the FOMBT is favored at small scattering angles below 30°, whereas the DWBA provides a better description at scattering angles above 30°.

The experimentally determined parameters are presented in Table 7.1.3.

Figure 7.1.6 shows the experimentally determined and theoretically calculated values of the alignment angle γ and the linear polarization P_{lin}^+ for the excitation of "$^3P_1$" state in Kr at 50 eV. The alignment angle depicted in Figure 7.1.6 reflects essentially the same good agreement between experiment and theories, again favoring the FOMBT at small scattering angles below 25° and favoring the DWBA at scattering angles above 30°. The comparison for P_{lin}^+ parameter on the other hand, is not very meaningful due to the comparatively large uncertainties.

A comparison between the data for Ne, Ar and Kr at same electron impact energy of 50 eV shows generally good agreement at small scattering angles where they display the same general trend as a function of θ_e. Both parameters decline from the forward direction to a minimum. The angular position of the minimum is shifted systematically towards smaller scattering angle as one goes from Ne to Ar to Kr, i.e. with increasing complexity of the target atom. The measured parameters in Kr show perhaps the best agreement between experiment and the DWBA and the FOMBT predictions. For Ne and Ar at 50 eV the agreement is generally less satisfactory, in particular in Ne, where there is an abrupt disagreement above about 30°. The same behavior was also observed by Khahoo and McConkey [1986, 1987] for Ne at 80 eV. The alignment angle γ is a parameter which is perhaps least sensitive to the details of the collision process. The comparison of experimentally determined and theoretically

Table 7.1.3: Coherence parameters P_1 and P_2 for excitation of the $5s[3/2]_{J=1}$ state in Kr at an impact energy of 50 eV and various electron scattering angles. Given are the nominal values of P_1 and P_2 corrected for all instrumental effects, where necessary, along with the extracted values for the alignment angle γ and the linear polarization P^+_{lin}. The quoted errors include all systematic uncertainties and one standard deviation of counting statistics.

Scattering angle (deg)	P_1 Parameter	P_2 Parameter	Alignment angle γ (deg)	linear Polarization P^+_{lin}
5.0±2.5	0.21±0.15	-0.85±0.17	-38.1±6.1	0.88±0.20
10.0±2.5	-0.42±0.14	-0.73±0.18	-60.0±7.1	0.84±0.23
15.0±2.5	-0.84±0.14	-0.21±0.06	-83.0±3.0	0.87±0.15
20.0±2.5	-0.50±0.12	0.23±0.11	77.7±47.8	0.55±0.15
25.0±2.5	0.29±0.09	0.32±0.12	23.9±9.8	0.43±0.15
30.0±2.5	0.87±0.11	-0.34±0.14	-10.7±5.2	0.93±0.15
35.0±2.5	0.78±0.17	-0.35±0.14	-12.1±6.6	0.85±0.21
40.0±2.5	0.74±0.14	-0.71±0.15	-21.9±5.7	1.03±0.20

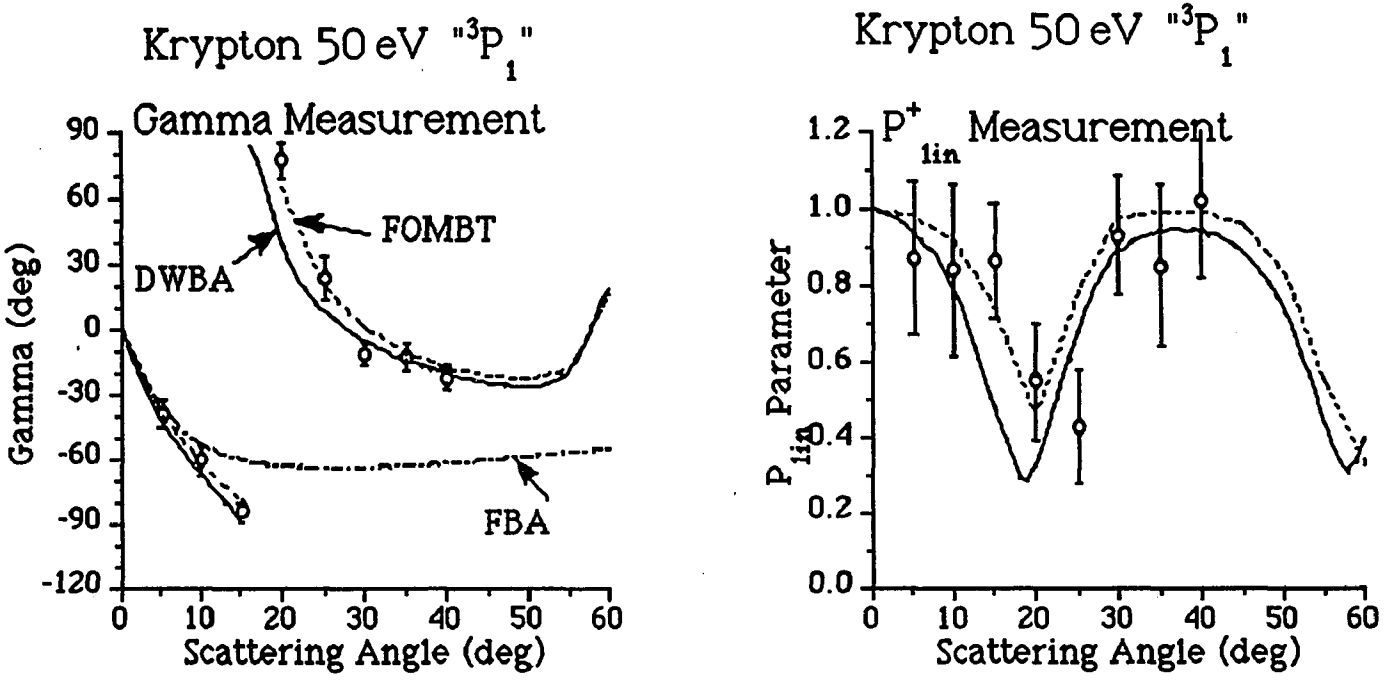

Figure 7.1.6: Alignment angle γ and linear polarization P^{+}_{lin} for excitation of the $5s[3/2]_{J=1}$ state in Kr at 50 eV as a function of electron scattering angle. Error bars include all known systematic uncertainties and one standard deviation of counting statistics. Where no error bar is indicated, the uncertainty is smaller than the plot symbol. For clarity, no horizontal error bars are indicated.

predicted P_{lin}^{+} parameter seems to favor the DWBA at least in Ne and Ar where a meaningful comparison is possible.

In summary, we find that the DWBA and the FOMBT seem to provide an adequate description of the measured P_1 and P_2 coherence parameters at large impact parameters (intermediate impact energy of 50 eV and small scattering angles). There is evidence for a gradual break-down of these first-order models as one goes to large scattering angles (i.e. smaller impact parameters). Furthermore, there is evidence for a target-specific component in the theoretical descriptions. These first-order perturbative approaches appear to work better for more complex target (Ar and Kr), where details of the inelastic scattering process which are not incorporated into these models seem to play a less prominent role than in Ne.

§7.2 Excitation of the $4s'[1/2]^0_1$ State in Ar at 50 eV, 40 eV, 30 eV, and 25 eV

This sequence of measurements was carried out in an effort to investigate a possible dependence of the level of a agreement between experiment and theory on the impact energy.

The measured P_1 and P_2 parameters for the excitation of $4s'[1/2]^0_1$ ("$^1P_1$") state in Ar at various electron impact energies (50 eV, 40 eV, 30 eV and 25 eV) along with the theoretical predictions (FBA, DWBA and FOMBT) are shown in the following figures:

1) figure 7.1.3, impact energy of 50 eV and scattering angles up to 40°

2) figure 7.2.1, impact energy of 40 eV and scattering angles up to 50°

3) figure 7.2.3, impact energy of 30 eV and scattering angles up to 40°

4) figure 7.2.5, impact energy of 25 eV and scattering angles up to 55°

No FOMBT prediction has been included in figures 7.2.1 and 7.2.5, since such calculations do not exist. A close look at figure 7.2.1 which shows the measured and calculated P_1 and P_2 parameters at 40 eV shows that P_1 follows the general feature predicted by the DWBA similar to what was observed at 50 eV (figure 7.3.1), but all measured P_1 data seem to be shifted systematically towards larger electron scattering angle relative to the DWBA prediction by up to 5°. The values of the measured P_2 parameter show a similar trend. In view of the uncertainty of the electron scattering angle (±2.5°), the apparent shift of the measured P_1 and P_2 parameters towards larger scattering angle relative to the theoretical prediction could be somewhat exaggerated. However, looking at figure 7.2.3 for 30 eV, we find that the measured P_1 and P_2

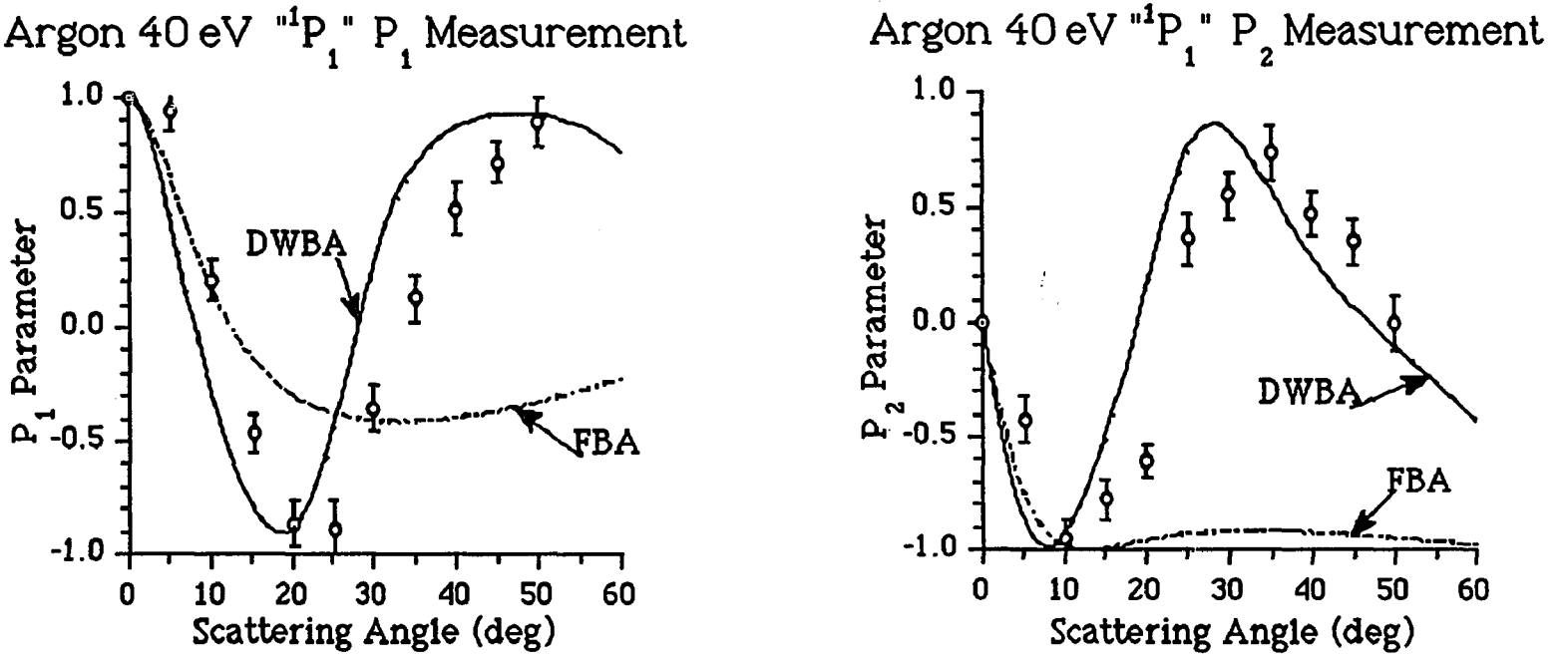

Figure 7.2.1: P_1 and P_2 polarization correlation parameters for excitation of the $4s'[1/2]_{J=1}$ state in Ar at 40 eV as a function of electron scattering angle. Error bars include all known systematic uncertainties and one standard deviation of counting statistics. For clarity, no horizontal error bars are indicated.

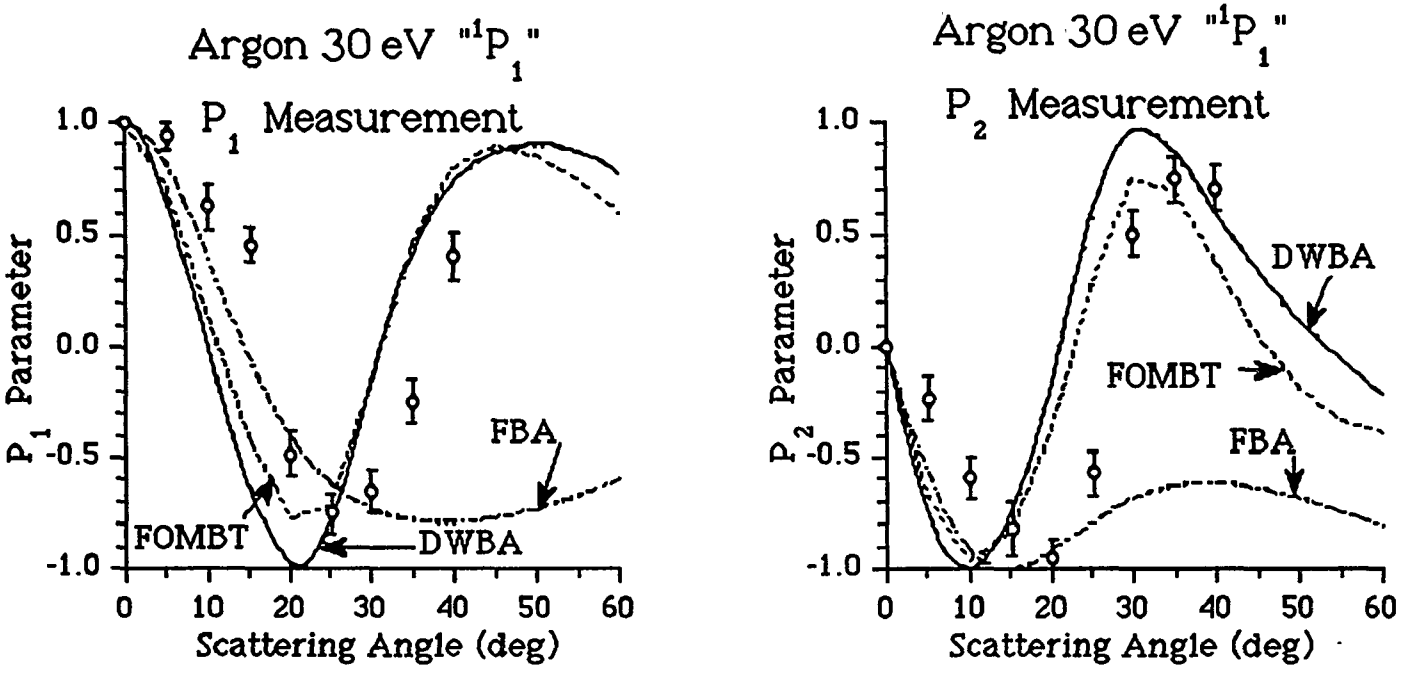

Figure 7.2.3: P_1 and P_2 polarization correlation parameters for excitation of the $4s'[1/2]_{J=1}$ state in Ar at 30 eV as a function of electron scattering angle. Error bars include all known systematic uncertainties and one standard deviation of counting statistics. For clarity, no horizontal error bars are indicated.

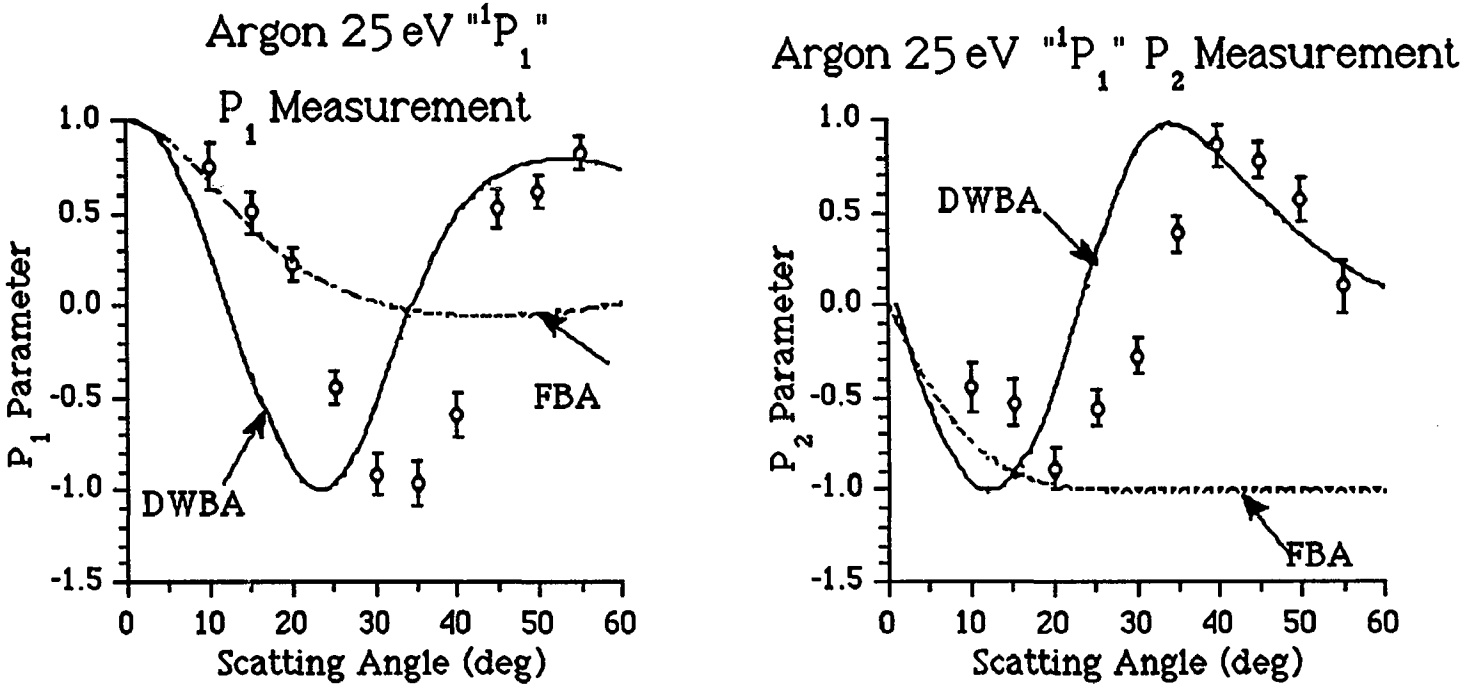

Figure 7.2.5: P_1 and P_2 polarization correlation parameters for excitation of the $4s'[1/2]_{J=1}$ state in Ar at 25 eV as a function of electron scattering angle. Error bars include all known systematic uncertainties and one standard deviation of counting statistics. For clarity, no horizontal error bars are indicated.

parameters again follow the general feature predicted by the theories, but appear to be shifted towards larger scattering angle relative to the theoretical predictions even more than at 40 eV. The shift of the measured P_1 and P_2 parameters towards larger scattering angle at 30 eV is about 8°. The experimentally determined P_1 and P_2 parameters of figure 7.1.3 at 50 eV which was discussed in the last section also showed a small, but much less, pronounced shift towards larger scattering relative to the theoretical predictions (2° at most). Such a shift could be entirely due to the uncertainty is the scattering angle of 2.5° (or caused by a slight shift in the horizontal alignment of the electron beam in the scattering plane).

The measured and calculated P_1 and P_2 parameters of figure 7.2.5 at 25 eV further underscore the notion that the measured P_1 and P_2 parameters are shifted towards larger scattering angle relative to the theoretical prediction as one goes to lower impact energies. Here the shift is about 10°.

We also note that this shift towards larger scattering angles is largely restricted to the scattering angle region below 40°, whereas at larger scattering angles the experimental data seem to approach the theoretical curves. Further measurements at larger scattering angles would be desirable to investigate this trend further.

In summary, the comparison of the experimentally measured and the theoretically predicted P_1 and P_2 parameters at electron impact energies 50 eV, 40 eV, 30 eV and 25 eV for "$^1P_1$" excitation in Ar showed a systematic and gradually increasing shift of the measured data towards larger scattering angles relative to the theoretical predictions with decreasing electron impact energy. This appears to be a characteristic signature of the gradual break-down of the first-order perturbative theories. A similar observation was reported by Gough et al. [1991] in their angular correlation

study of the excitation of $5s[3/2]^0_1$ state in Kr at 15 eV and by McConkey and collaborators [1991] in a polarization correlation study of the excitation of $4s[3/2]^0_1$ ("$^3P_1$") state in Ar at 20 eV.

The experimentally determined and theoretically predicted values of the alignment angle γ and the linear polarization P_{lin}^+ extracted from P_1 and P_2 parameters are shown in figures:

1) figure 7.1.4, impact energy of 50 eV, scattering angles up to 40°

2) figure 7.2.2, impact energy of 40 eV, scattering angles up to 50°

3) figure 7.2.4, impact energy of 30 eV, scattering angles up to 40°

4) figure 7.2.6, impact energy of 25 eV, scattering angles up to 55°

The deviations between the experimentally determined and theoretically predicted values of the alignment angle γ for various electron impact energies show the same signature that was found for the P_1 and P_2 parameters. The values of the experimentally determined alignment angle γ appear to be shifted towards larger scattering angle relative to the theoretical predictions, and the shift gets larger with decreasing electron impact energy. However, the shift towards larger scattering angles for the alignment angle γ is less prominent than that for the individual P_1 and P_2 parameters, i.e. in the case of 25 eV, the shift for the alignment angle is about 7°-8°, which is slightly less than 10° observed for the individual P_1 and P_2 parameters. Even though this difference in the shift is about the size of the uncertainty in the electron scattering angle, the shift is systematically smaller for γ rather than fluctuate randomly by 2.5°. This is further evidence that the alignment angle is perhaps a less sensitive measure of the level of agreement and disagreement between experiment

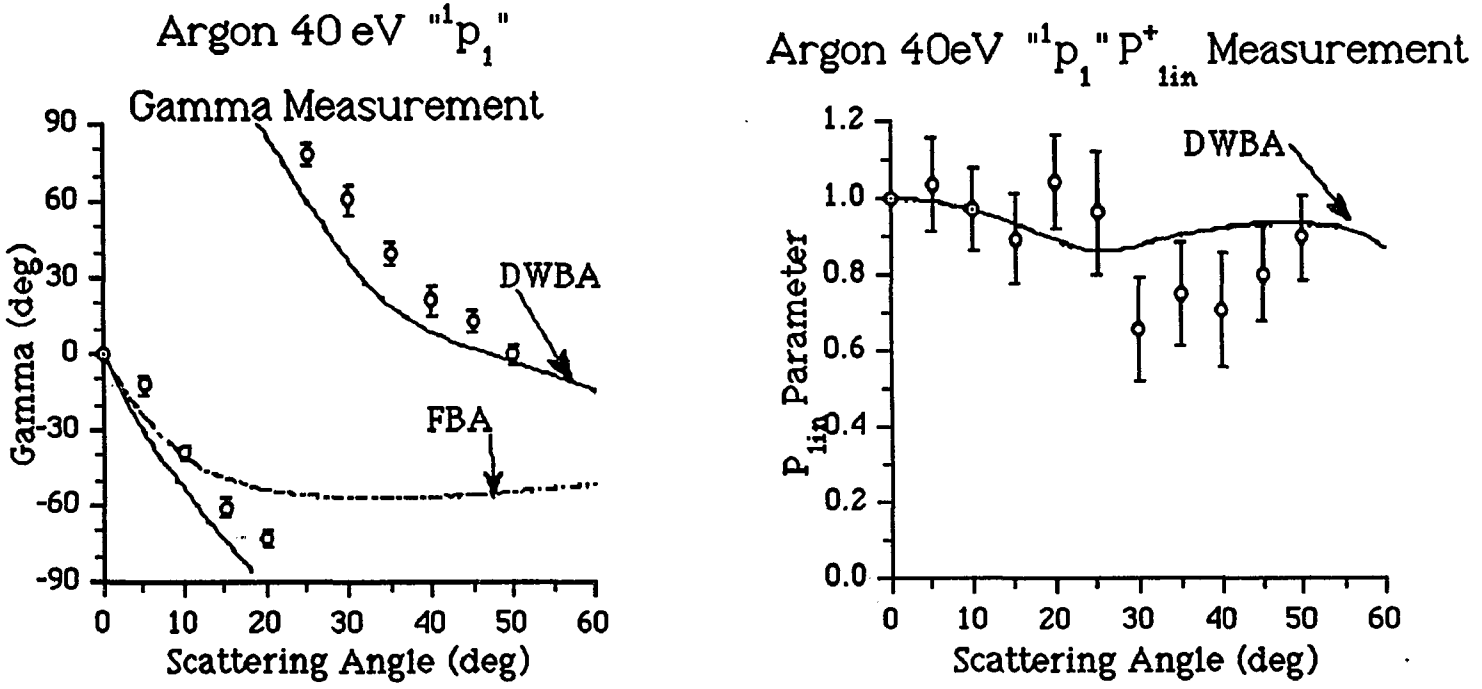

Figure 7.2.2: Alignment angle γ and linear polarization P^+_{lin} for excitation of the $4s'[1/2]_{J=1}$ state in Ar at 40 eV as a function of electron scattering angle. Error bars include all known systematic uncertainties and one standard deviation of counting statistics. For clarity, no horizontal error bars are indicated.

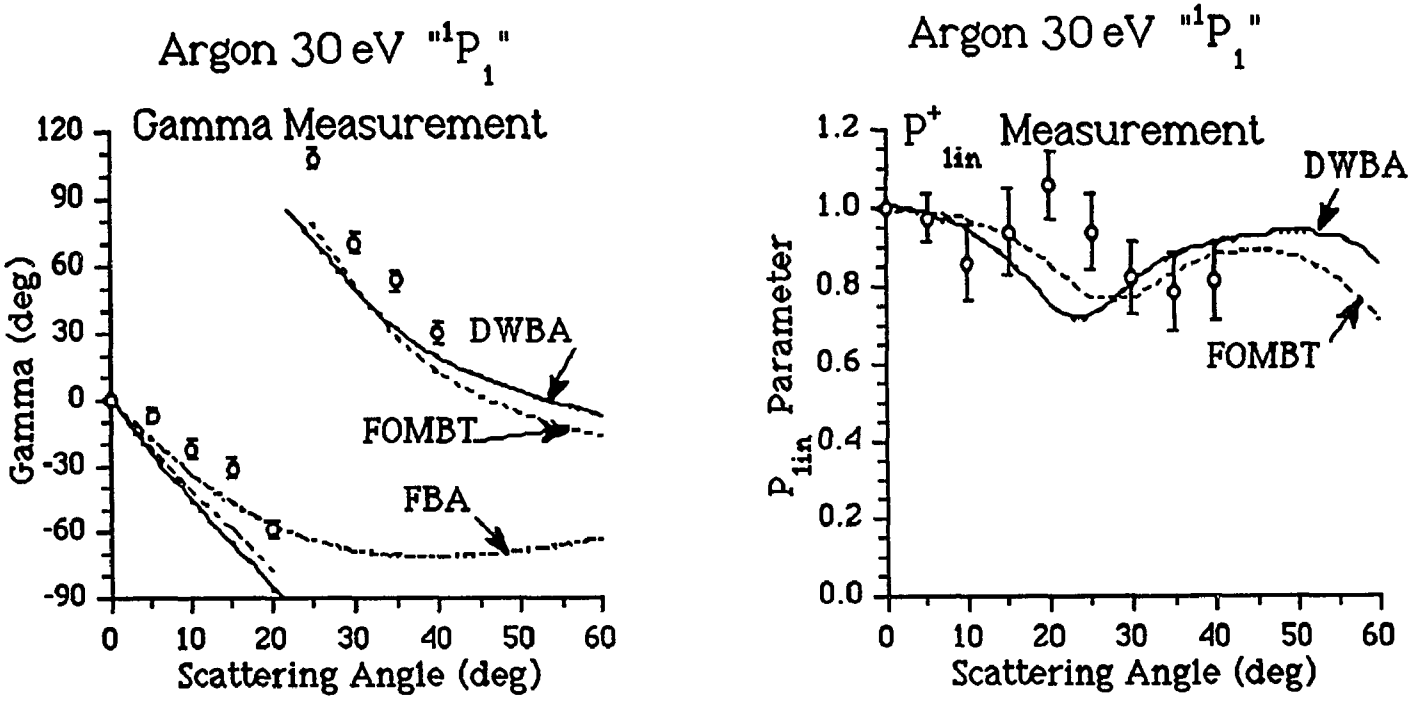

Figure 7.2.4: Alignment angle γ and linear polarization P^{+}_{lin} for excitation of the $4s'[1/2]_{J=1}$ state in Ar at 30 eV as a function of electron scattering angle. Error bars include all known systematic uncertainties and one standard deviation of counting statistics. For clarity, no horizontal error bars are indicated.

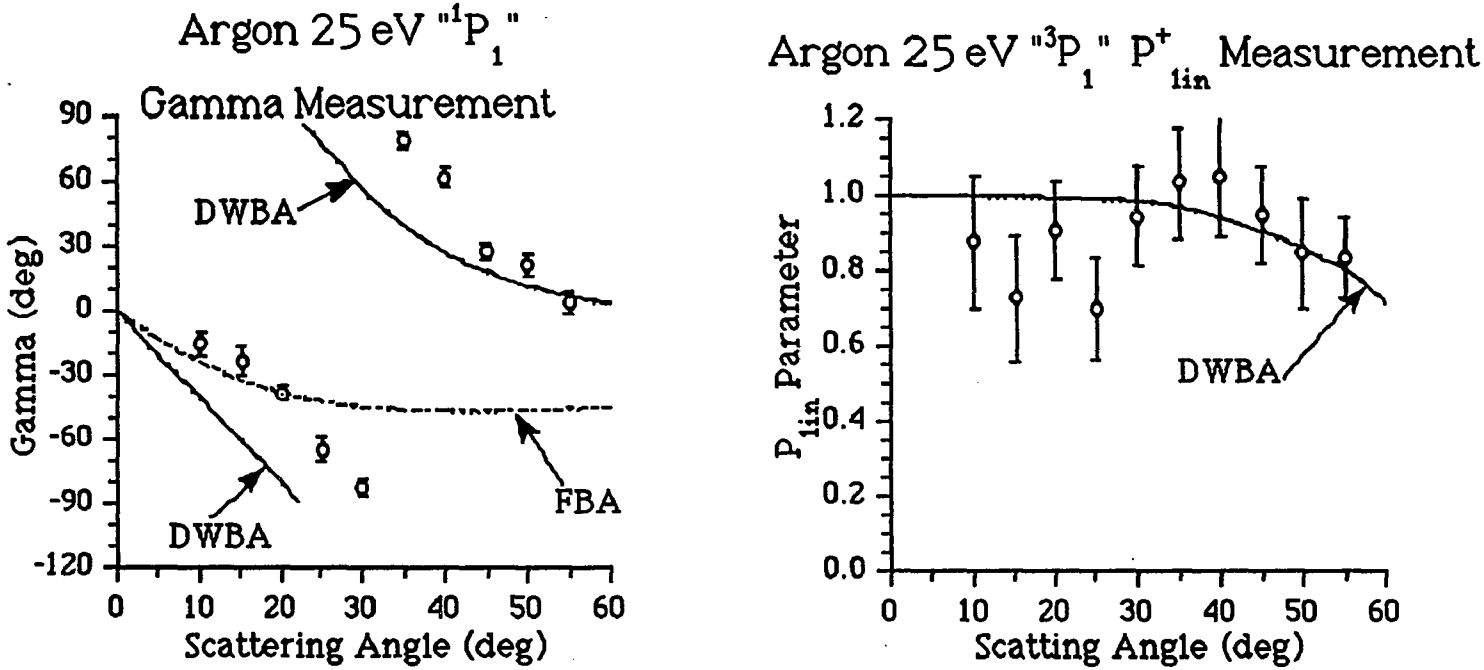

Figure 7.2.6: Alignment angle γ and linear polarization P^+_{lin} for excitation of the $4s'[1/2]_{J=1}$ state in Ar at 25 eV as a function of electron scattering angle. Error bars include all known systematic uncertainties and one standard deviation of counting statistics. For clarity, no horizontal error bars are indicated.

and theory.

The comparison of experimentally determined and theoretically predicted values of the linear polarization P_{lin}^{+} at 50 eV was presented in the previous section. The experimentally determined values of P_{lin}^{+} parameter were found to favor the DWBA at large scattering angles. For the P_{lin}^{+} parameters at 40 eV and 30 eV, that trend is less apparent. The experimentally determined P_{lin}^{+} parameters are shifted towards larger scattering angle relative to the theoretically predicted ones and appear to approach the theoretical predictions at scattering angles above 35°. For the P_{lin}^{+} parameter at 25 eV, a reasonably good agreement between the experimentally determined and theoretically predicted P_{lin}^{+} values is apparent above 30°, whereas the small angle values are consistently smaller than the theoretical prediction $P_{lin}^{+} \approx 1$.

All experimentally determined parameters are summarized in Table 7.1.2 (50 eV), Table 7.2.1 (40 eV), Table 7.2.2 (30 eV) and Table 7.2.3 (25 eV).

Table 7.2.1: Coherence parameters P_1 and P_2 for excitation of the $4s'[1/2]_{J=1}$ state in Ar at an impact energy of 40 eV and various electron scattering angles. Given are the nominal values of P_1 and P_2 corrected for all instrumental effects, where necessary, along with the extracted values for the alignment angle γ and the linear polarization P^+_{lin}. The quoted errors include all systematic uncertainties and one standard deviation of counting statistics.

Scattering angle (deg)	P_1 Parameter	P_2 Parameter	Alignment angle γ (deg)	linear Polarization P^+_{lin}
5.0±2.5	0.95±0.09	-0.42±0.10	-12.0±3.5	1.04±0.12
10.0±2.5	0.21±0.09	-0.95±0.09	-38.8±3.2	0.97±0.11
15.0±2.5	-0.46±0.08	-0.77±0.09	-60.4±3.7	0.90±0.12
20.0±2.5	-0.86±0.10	-0.60±0.07	-72.5±3.1	1.05±0.12
25.0±2.5	-0.89±0.13	0.37±0.11	78.7±4.5	0.96±0.16
30.0±2.5	-0.35±0.10	0.56±0.10	61.0±6.0	0.66±0.14
35.0±2.5	0.13±0.10	0.74±0.12	40.0±4.5	0.75±0.14
40.0±2.5	0.52±0.11	0.48±0.10	21.4±6.0	0.71±0.15
45.0±2.5	0.72±0.09	0.36±0.10	13.3±4.6	0.80±0.13
50.02.5	0.90±0.11	0.00±0.12	0.0±3.8	0.90±0.11

Table 7.2.2: Coherence parameters P_1 and P_2 for excitation of the $4s'[1/2]_{J=1}$ state in Ar at an impact energy of 30 eV and various electron scattering angles. Given are the nominal values of P_1 and P_2 corrected for all instrumental effects, where necessary, along with the extracted values for the alignment angle γ and the linear polarization P^+_{lin}. The quoted errors include all systematic uncertainties and one standard deviation of counting statistics.

Scattering angle (deg)	P_1 Parameter	P_2 Parameter	Alignment angle γ (deg)	linear Polarization P^+_{lin}
5.0±2.5	0.95±0.06	-0.23±0.10	-6.8±3.3	0.98±0.08
10.0±2.5	0.63±0.10	-0.59±0.09	-21.6±4.5	0.86±0.13
15.0±2.5	0.46±0.08	-0.82±0.12	-30.4±3.9	0.94±0.14
20.0±2.5	-0.48±0.10	-0.95±0.08	-58.4±3.4	1.06±0.12
25.0±2.5	-0.75±0.09	-0.57±0.10	71.4±4.1	0.94±0.13
30.0±2.5	-0.65±0.09	0.51±0.10	70.9±4.7	0.83±0.13
35.0±2.5	-0.24±0.10	0.75±0.10	53.9±4.5	0.79±0.13
40.0±2.5	-0.41±0.11	0.71±0.10	30.0±5.1	0.82±0.14

Table 7.2.3: Coherence parameters P_1 and P_2 for excitation of the $4s'[1/2]_{J=1}$ state in Ar at an impact energy of 25 eV and various electron scattering angles. Given are the nominal values of P_1 and P_2 corrected for all instrumental effects, where necessary, along with the extracted values for the alignment angle γ and the linear polarization P^+_{lin}. The quoted errors include all systematic uncertainties and one standard deviation of counting statistics.

Scattering angle (deg)	P_1 Parameter	P_2 Parameter	Alignment angle γ (deg)	linear Polarization P^+_{lin}
5.0±2.5	---	---	---	---
10.0±2.5	0.76±0.13	-0.44±0.13	-15.0±5.8	0.88±0.18
15.0±2.5	0.51±0.11	-0.52±0.13	-22.8±6.7	0.73±0.17
20.0±2.5	0.23±0.09	-0.88±0.11	-37.7±3.6	0.91±0.13
25.0±2.5	-0.44±0.09	-0.55±0.10	-64.3±5.4	0.70±0.13
30.0±2.5	-0.91±0.11	-0.27±0.10	-81.7±3.8	0.95±0.13
35.0±2.5	-0.96±0.12	0.39±0.10	78.9±3.8	1.04±0.15
40.0±2.5	-0.59±0.12	0.87±0.11	62.1±4.4	1.05±0.16
45.0±2.5	0.53±0.10	0.79±0.09	28.1±4.0	0.95±0.13
50.0±2.5	0.62±0.09	0.58±0.12	21.5±5.0	0.85±0.15
55.0±2.5	0.83±0.09	0.11±0.14	3.8±5.2	0.84±0.11

§7.3 Excitation of the $5s[3/2]^0_1$ State in Kr at 30 eV

This series of measurement was carried out to check whether the apparent disagreement between experiment and theory that was observed in Ar at 30 eV and 25 eV is target-specific.

The measured P_1 and P_2 parameters for the excitation of $5s[3/2]^0_1$ "$^3P_1$" state in Kr at an electron impact energy of 30 eV along with the theoretical predictions (FBA, DWBA and FOMBT) are shown in figure 7.3.1. The experimentally determined values of the alignment angle γ and the linear polarization P_{lin}^+ along with the theoretical predictions are shown in figure 7.3.2.

We found generally very good agreement between experimentally measured and theoretically predicted P_1 and P_2 parameters for excitation of the Kr "$^3P_1$" state at an electron impact energy of 30 eV up to scattering angles of 55°. The comparison between experimentally measured and theoretically predicted P_1 and P_2 parameters for the excitation of "$^3P_1$" state in Kr at 30 eV reaffirms to some extent the trend observed at 50 eV, that is that the FOMBT prediction is favored at scattering angles below 30°, whereas the DWBA is favored at scattering angles above 30°. The alignment angle γ, extracted from the P_1 and P_2 parameters, for the excitation of "$^3P_1$" state in Kr at 30 eV also shows that the FOMBT is favored at small scattering angles, whereas the DWBA is favored at large angles. The linear polarization P_{lin}^+ for the excitation of "$^3P_1$" state in Kr at 30 eV provides little new information. Also shown are the experimental data measured in the angular correlation experiment at the same electron impact energy by Crowe and collaborators. The angular correlation results agree in general rather well with our polarization correlation data except

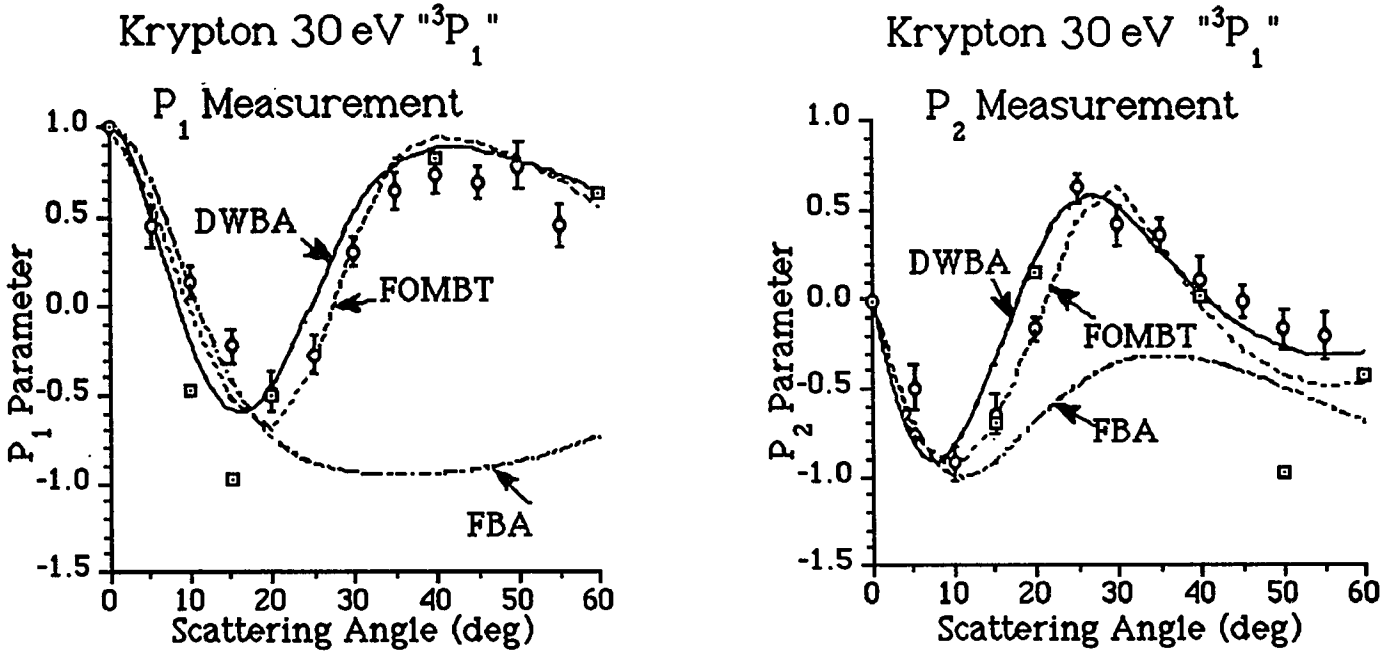

Figure 7.3.1: P_1 and P_2 polarization correlation parameter for excitation of the $5s[3/2]_{J=1}$ state in Kr at 30 eV as a function of electron scattering angle. Error bars include all known systematic uncertainties and one standard deviation of counting statistics. For clarity, no horizontal error bars are indicated. The squares (□) denote P_1 and P_2 values extracted from the angular correlation studies of Murray et al. [1990]. No error bars are given for the data of angular correlation measurements.

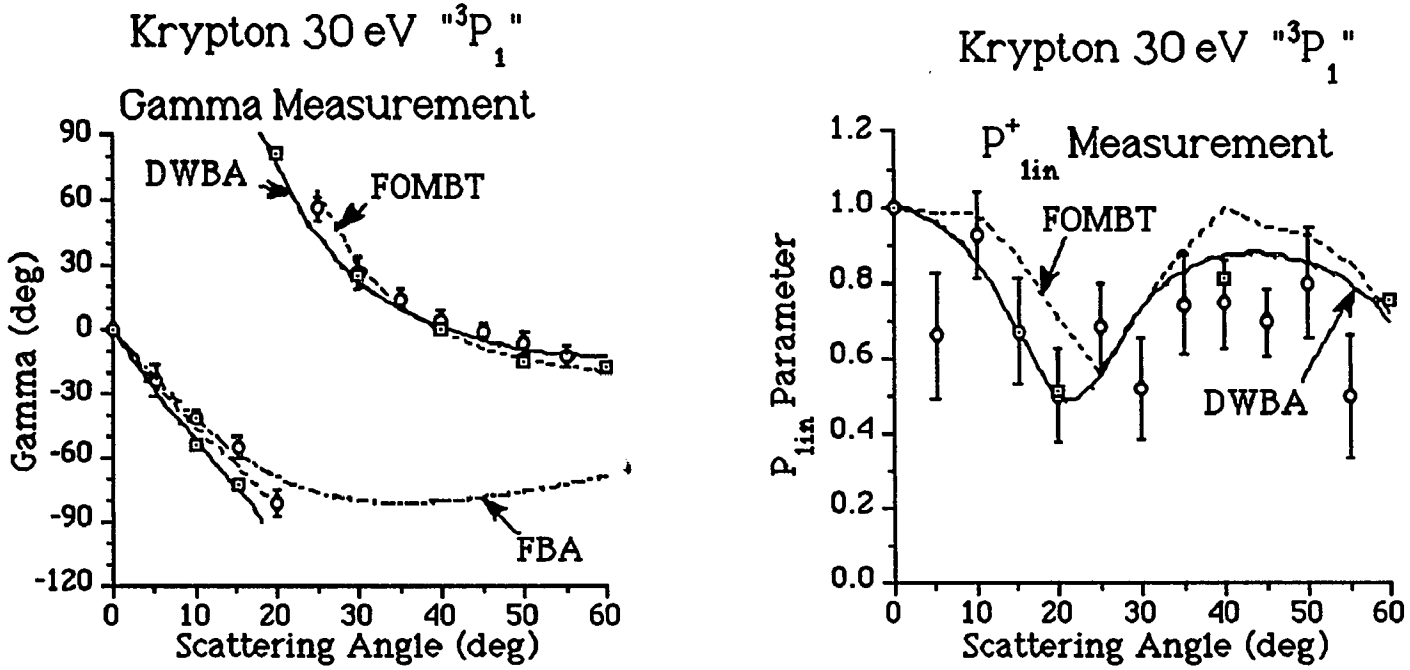

Figure 7.3.2: Alignment angle γ and linear polarization P^{+}_{lin} for excitation of the $5s[3/2]_{J=1}$ state in Kr at 30 eV as a function of electron scattering angle. Error bars include all known systematic uncertainties and one standard deviation of counting statistics. For clarity, no horizontal error bars are indicated. The squares (□) denote P_1 and P_2 values extracted from the angular correlation studies of Murray et al. [1990]. No error bars are given for the data of angular correlation measurements.

in a few cases. It has been suggested [Crowe 1992, private communication] that some of the angular correlation data might have been affected by instrumental and other effects as discussed in the review of Becker et al. [1992].

It is noteworthy to state that the good agreement between experiment and theory in the case of the Kr "$^3P_1$" excitation at 30 is contrary to the comparatively much poorer agreement in the case of the Ar "$^1P_1$" excitation at the same energy. This might indicate that there is a target-specific component in the theoretical description that is handled better for the heavier target.

The experimentally determined parameters are listed in Table 7.3.1.

Table 7.3.1: Coherence parameters P_1 and P_2 for excitation of the $5s[3/2]_{J=1}$ state in Ar at an impact energy of 30 eV and various electron scattering angles. Given are the nominal values of P_1 and P_2 corrected for all instrumental effects, where necessary, along with the extracted values for the alignment angle γ and the linear polarization P^+_{lin}. The quoted errors include all systematic uncertainties and one standard deviation of counting statistics.

Scattering angle (deg)	P_1 Parameter	P_2 Parameter	Alignment angle γ (deg)	linear Polarization P^+_{lin}
5.0±2.5	0.45±0.12	-0.49±0.12	-23.7±7.3	0.67±0.17
10.0±2.5	0.14±0.09	-0.92±0.10	-40.7±3.2	0.93±0.11
15.0±2.5	-0.22±0.10	-0.64±0.11	-54.5±65.5	0.68±0.14
20.0±2.5	-0.48±0.11	-0.16±0.07	-80.8±5.7	0.51±0.13
25.0±2.5	-0.27±0.11	0.63±0.08	56.6±5.5	0.69±0.12
30.0±2.5	0.31±0.08	0.42±0.11	26.8±7.1	0.52±0.14
35.0±2.5	0.65±0.10	0.37±0.09	14.8±4.9	0.75±0.13
40.0±2.5	0.74±0.10	0.12±0.12	4.6±5.1	0.75±0.12
45.0±2.5	0.70±0.09	-0.01±0.09	-0.4±3.7	0.70±0.09
50.0±2.5	0.79±0.13	-0.16±0.11	-5.7±4.7	0.80±0.15
55.0±2.5	0.46±0.12	-0.20±0.14	-11.7±5.0	0.50±0.17

§7.4 Summary and Further Directions

A comparison between experimentally measured coherence parameters and theoretical predictions has been carried out for the electron impact excitation of the heavy noble gases Ne, Ar and Kr. At an impact energy of 50 eV in neon and argon, we found good agreement between experiment and theory at small scattering angles and somewhat less satisfactory agreement at larger scattering angles. At 50 eV in krypton, we found good agreement between experiment and theory at scattering angles up to 40°. In argon at impact energies below 50 eV, we found a systematic and gradual shift of the measured coherence parameters towards larger scattering angles relative to the theoretical prediction. The shift increased with decreasing electron energy. This appears to be a characteristic signature of the gradual break-down of first-order perturbative theories as one goes to lower impact energies. The very good agreement between experiment and theory in krypton at an impact energy of 30 eV might indicate that there is a target-specific component that influences the level of agreement between experiment and theory. We also found that the alignment angle γ, which is extracted from the linear polarization correlation parameters P_1 and P_2, is perhaps rather insensitive to the details of the collision process. For the linear polarization parameter P^+_{lin}, we found that the DWBA provides a better description in most cases than FOMBT.

Further work should evolve along two lines. Firstly, studies of heavy noble gas excitation using spin polarized incident electron in an effort to unravel further details regarding spin-dependent interaction in the excitation process. Secondly, work involving unpolarized incident electron which should focus on the measurement of the circular polarization correlation parameter P_3 and in general on the measurement of

coherence parameters for low impact energies (preferably below the first ionization threshold) and for large scattering angles in effort to stimulate theoretical work that goes beyond perturbation-type calculation.

Bibliography

Andersen, Gallagher and Hertel, Phys. Rep. **165**, 1(1988)

Arriola, Teubner, Ugbabe and Weigold, J. Phys. B: At. Mol. Phys. **8**, 1275(1975)

Becker, Crowe and McConkey, J. Phys. B: At. Mol. Opt. Phys. **25**, 3885(1992)

Bederson, Comments At. Mol. Phys. **1**, 41 and 65(1969)

Bederson, *Atomic Physics*, eds. Smith and Walters (Plenum New York, 1973) p401

Beijers, van den Brink, van Eck and Heideman, J. Phys. B: At. Mol. Phys. **19**, L581(1986)

Bevington, *Data Reduction and Error Analysis for the Physical Sciences* (McGraw-Hill, New York, 1969)

Blum, *Density Matrix Theory and Application* (Plenum Press, New York and London, 1981)

Bransden and Joachain, *Physics of Atoms and Molecules* (Longman Group Limited, 1983)

Bransden and McDowell, Phys. Rep. **30**, 3(1977)

Brunt, King and Read, J. Phys. B: At. Mol. Phys. **10**, 3781(1977)

van der Burgt, Corr and McConkey, J. Phys. B: At. Mol. Opt. Phys. **24**, 1409(1991)

Cartwright and Csanak, J. Phys. **B20**, L583(1987)

Clausing, Z. Phys. **66**, 471(1931)

Corr, Plessis and McConkey, Phys. Rev. **A42**, 5240(1990)

Corr, van der Burgt, Plessis, Khakoo, Hammond and McConkey, J. Phys. B: At. Mol. Opt. Phys. **24**, 1069(1991)

Csanak and Cartwright, J. Phys. B: At Mol. Phys. **22**, 2769(1989)

Csanak, Taylor and Tripathy, J. Phys. B: At. Mol. Phys. **6**, 2040(1973)

Csanak, Taylor and Yaris, a: Phys. Rev. **A3**, 1322(1971), b: Adv. Atom. Molec. Phys. **7**, 287(1970)

Csanak and Meneses, Private Communication

Danjo, Koike, Kani, Sugahara, Takahashi and Nshimura, J. Phys. B: At. Mol. Phys. **18**, L595(1985)

da Paixao, Padial and Csanak, Phys. Rev. **A30**, 1697(1984)

da Paixao, Padial, Csanak and Blum, Phys. Rev. Lett. **45**, 1164(1980)

Edmonds, *Angular Momentum in Quantum Mechanics* (Princeton University Press, 1957)

Eisberg and Resnick, *Quantum Physics of Atoms, Molecule, Solids, Nulei, and Particales* (Wiley, New York, 1985)

Eminyan, MacAdam, Slevin and Kleinpoppen, Phys. Rev. Lett. **31**, 576(1973)

Eminyan, MacAdam, Slevin, Standage and Kleinpoppen, J. Phys. B: At Mol. Phys. **7**, 1597(1974)

Fano and Macek, Rev. Mod. Phys. **45**, 553(1973)

Fano and Racah, *Irreducible Tensorial Sets* (Academic, New York, 1959)

Feynman, *The Feynman Lecture on Physics* (Reading, Mass Addison-Wesley Pub. Co., 1963-65)

Frank and Hertz, Verhand, Deut. Physik Ges. **16**, 512(1914)

Giordmaine and Wang, Appl. Phys. **31**, 463(1960)

Goldberger and Watson, *Collision Theory* (John Wiley & Sons, Inc., 1964)

Gough, Murray, Crowe, Proc. 17th Int. Conf. on the Physics of Electronic and Atomic Collision (Brisbane), ed McCarthy, MacGillivray and Standage (Brisbane: Griffith University Press, 1991) p.123

Hammond, Karras, and McConkey, Phys. Rev. **A40**, 1804(1989)

Harting and Read, *Electrostatic Lenses* (Elsevier, New York, 1976)

Heddle and Gallagher, Rev. Mod. Phys. **61**, 221(1989)

Hertel and Stoll, J. Phys. B**7**, 570(1974)

Kessler, Electron-Polarization Phenomena in Electron-Atom Collision, Advances in At., Mol., and Opt. Phys. V.27,81(1991) (Academic Press, Inc, 1991)

Kennard, *Kinetic Theory of Gases* (McGraw Hill, New York, 1938)

Khakoo and McConkey, Phys. Rev. Lett. **57**, 679(1986), J. Phys. B: At. Mol. Phys. **20**, 5541(1987)

King, Neill and Crowe, J. Phys. B: At. Mol. Phys. **18**, L589(1985)

Knudsen, Ann. Physik **28**, 75(1909)

Lichtenberg, *Unitary Symmetry and Elementary Particles* (Academic Press, New York 1978)

Macek and Jaeck, Phys. Rev. **A4**, 2288(1971)

Machado, Leal and Csanak, J. Phys. B: At. Mol. Phys. **15**, 1773(1982), Phys. Rev. **A29**, 1811(1984)

Machado, Meneses, Csanak and Cartwright, Proc. 17th Int. Conf. on the Physics of Electronic and Atomic Collision (Brisbane), ed McCarthy, MacGillivray and Standage (Brisbane: Griffith University Press, 1991) p.127

Malcolm and McConkey, J. Phys.b: At. Mol. Phys. **12**, 511(1979)

Martus and Becker, J. Phys. B: At. Mol. Opt. Phys. **22**, L497(1989)

Martus, Becker and Madison, Phys. Rev. **A38**, 4876(1988)

Martus, Zheng and Becker, Phys. Rev. **A44**, 1682(1991)

Matthias et al., Chem. Phys. Lett. **52**, 139(1977)

McConkey, Crouch and Tomc, Appl. Opt. **21**, 1643(1982)

McConkey and collaborators, Private Communication

McGregor, Hils, Hippler, Malik, Williams, Zaidi and Kleinpoppen, J. Phys. B: At. Mol. Phys. **15**, L411(1982)

Meneses, *da* Paixão and Padial, Phys. Rev. **A32**, 156(1985)

Meneses, Csanak and Cartwright, Proc. 17th Int. Conf. on the Physics of Electronic and Atomic Collision (Brisbane), eds McCarthy, MacGillivray and Standage (Brisbane: Griffith University Press) p.129

Moiseiwitsch and Smith, Rev. Mod. Phys. **40**, 238(1968)

Mott and Massey, *The Theory of Atomic Collisions* (Clarendon Press, Oxford, 1987)

Murray, Gough, Neill and Crowe, J. Phys. B: At. Mol. Opt. Phys. **23**, 2137(1990)

Nishimura, Danjo and Takahashi, J. Phys. B: At. Mol. Phys. **19**, L167(1986)

Olander and Kruger, J. Appl. Phys. **41**, 2769(1970)

Percival and Seaton, Philos. Trans. R Soc. London **A251**, 113(1958)

Pochat, Gelebart and Peresse, J. Phys. B: At. Mol. **13**, L79(1980)

Ramsauer, a: Annalend Physik **64**, 513(1921), b: Annalend Physik **66**, 546(1921)

Ramsay, *Molecular Beam* (Oxford, Clarendon Press, 1956)

Rotenberg, Bivins, Metropolis and Wooten, *The 3-j and 6-j Symbols* (Technology Press, MIT, Cambridge, 1959)

Rubin, bederson, Goldstein and Collins, Phys. Rev. **282**, 182(1969)

Samson, *Techniques of Vacuum Ultraviolet Spectroscopy* (Pied Publications, Lincoln, Nebraska, 1967)

Schneider, Taylor and Yaris, Phys. Rev. **A1**, 855(1970)

Simon, Sohn, Hanne and Bartschat, J. Phys. B: At. Mol. Opt. Phys. **23**, L259(1990)

Slevin and Chwirot, J. Phys. B: At Mol Opt. Phys. **23**, 165(1990)

Smoluchowski, Ann. Physik **33**, 1559(1910)

Sobelman, *Atomic Spectra and Radiative Tansition*, Springer Series in Chemical Physics 1 (Springer-Verlag Berlin Heidelberg New York, 1979)

Sohn and Hanne, J. Phys. B: At. Opt. Phys. **25**, 4627(1992)

Srivastava, Katiyar and Rai, Phys. Rev. **A40**, 2749(1989)

Thomas, Csanak, Taylor, Yarlagadda, J. Phys. B: At. Mol. Phys. **7**, 1719(1974)

Townsend and Bailey, Phil. Mag. **43**, 593(1922)

Ugbabe, Teubner, Weigold and Arriola, J. Phys. B: At. Mol. Phys. **10**, 71(1977)

Uhrig Hanne, Kessler, Becker and Bartschat, Bull. APS, DAMOP (1993) in press

Vanderpoorten and Winters, J. Phys. B: At. Mol. Phys. **12**, 473(1979)

Walters, Phys. Rep. **116**, 1(1984)

Westerveld, Becker, Zetner, Corr and McConkey, Appl. Opt. **24**, 2256(1985)

Wykes, J. Phys. B: At. Mol. Phys. **5**, 1126(1972)

Zetner, Becker, Westerveld and McConkey, Appl. Opt. **23**, 3184(1984)

Zetner, Pradhan, Westerveld and McConkey, Appl. Opt. **22**, 2210(1983)

Zheng and Becker, Z. Phys. D: At. Mol. and Clus. **23**, 137(1992)

Zheng and Becker, J. Phys. B: At. Mol. Phys. **26**, 517(1993)

Zuegenmaier, Z. Angew. Phys. **64**, 184(1966)

Zuo, McEachran and Stauffer, J. Phys. B: At. Mol. Opt. Phys. **24**, 2853(1991)